This is the peer-reviewed, final accepted version for American Mineralogist, published by the Mineralogical Society of America.
The published version is subject to change. Cite as Authors (Year) Title. American Mineralogist, in press.
DOI: https://doi.org/10.2138/am-2022-8776. http://www.minsocam.org/

----------REVISION 1----------

Regular Article
Word Count: 9326 through Acknowledgements

Reconstructing diagenetic mineral reactions from silicified horizons of the Paleoproterozoic Biwabik Iron Formation, Minnesota

Samuel Duncanson[*1, 2], Latisha Brengman[1], Jena Johnson[3], Athena Eyster[4], John Fournelle[4], Aurélien Moy[4]

[1] Department of Earth and Environmental Sciences, University of Minnesota – Duluth, Duluth, MN, 55812, [2]Now at Department of Geological and Atmospheric Sciences, Iowa State University, Ames, IA 50011, [3] Department of Earth and Environmental Sciences, University of Michigan, Ann Arbor, MI 48109, [4] Department of Geoscience, University of Wisconsin Madison, Madison, WI 53706.

Email addresses: sdunc@iastate.edu* (SD) , lbrenmga@d.umn.edu (LB) , jenaje@umich.edu (JJ), aeyster@wisc.edu (AE), johnf@geology.wisc.edu (JF), amoy6@wisc.edu (AM)

Corresponding Author*: Sam Duncanson, Department of Geological and Atmospheric Sciences, Iowa State University, Ames, Iowa 50011 USA, Phone: 515-294-4477, Email: sdunc@iastate.edu

Keywords:
silicification, silica cementation, diagenesis, chamosite, greenalite

ABSTRACT

Primary phases in iron-rich chemical sedimentary rocks are important archives of seawater geochemistry throughout the Precambrian. The record of seawater chemistry, however, is obscured by post-depositional changes that occur during diagenesis, metamorphism, and modern weathering. Recent studies have identified silica-cemented horizons in some Archean and Paleoproterozoic iron formation that may preserve reduced, texturally early mineral phases, which may inform interpretations of oxygen dynamics preceding atmospheric oxygen accumulation before the ~2.3 Ga Great Oxidation Event (GOE). However, fewer investigations focus on silica-cemented horizons in Paleoproterozoic iron formation deposited after the GOE, a period where oxygen levels are poorly constrained. Here we present petrographic observations, scanning electron microscopy, electron microprobe analysis, and Raman spectroscopy from iron mineral phases preserved within silica-cemented horizons of the ~1.9 Ga Biwabik Iron Formation (Minnesota, United States) to constrain texturally early iron formation mineralogy from this crucial post-GOE interval. Based on textural relationships, the iron silicate greenalite is identified as the earliest-forming iron silicate mineral preserved within silica-cemented horizons. The magnesium- and aluminum-rich iron silicates chamosite and stilpnomelane are preserved proximal to fine-grained, non-silicified horizons, suggesting local geochemical exchange during early diagenesis. The presence of well-preserved, early-forming silicates containing predominantly ferrous iron may indicate reducing conditions at the sediment-water interface during deposition of the Biwabik Iron Formation. More definitively, future studies using iron silicate mineralogy as seawater geochemistry proxies should consider preservation by silica cementation, in addition to the effects of local geochemical exchange during diagenesis.

INTRODUCTION

Chemical sedimentary rocks, such as iron formations, archive geochemical conditions of marine environments throughout Earth history. Iron formations are iron and silica-rich chemical sedimentary rocks deposited throughout the Precambrian sedimentary record, notable for providing a record of marine (bio)geochemistry across the Archean-Proterozoic transition and the initial rise of atmospheric oxygen concentrations during the ~2.2-2.4 Ga Great Oxidation Event (GOE; Lyons et al. 2014; Gumsley et al. 2017; Poulton et al. 2021). Primary authigenic phases preserved in iron formations are of interest because they may record critical chemical information about the water column. Here, primary phases are defined as the earliest forming minerals that reflect geochemical conditions of the fluid at their time of precipitation. Following deposition, primary phases experience processes that alter and overprint original geochemical signatures including early and late diagenesis, burial, metasomatism and metamorphism, and modern weathering during fluid permeation and surface exposure (Klein 2005; Albut et al. 2018). Deciphering the mineralization histories and distinguishing these later secondary and tertiary mineral phases from primary phases is crucial for elucidating original geochemical information that can be linked to the depositing fluid and original depositional conditions.

Cementation by silica during early diagenesis may aid in mineral preservation by encapsulating precursor sediments near the time of silica precipitation, preventing subsequent major cation exchange and mineral transformations (Simonson 1987). Favorably, throughout most of the Precambrian, the lack of silica biomineral sinks likely resulted in high seawater silica concentrations at or above saturation (e.g., Siever 1992; Maliva et al. 2005), evidenced in part by deposition of abundant Si-rich chemical sedimentary rocks and widespread silicification (e.g., Brengman et al. 2020). Recent studies of silica-cemented horizons in iron formation identified

iron silicate inclusions, specifically Fe(II)-rich greenalite, and interpreted these minerals as primary precipitates reflective of anoxic depositional conditions (Rasmussen et al. 2013; Johnson et al. 2018; Muhling and Rasmussen 2020; Rasmussen et al. 2021 and references therein). The presence of putative primary greenalite within these silica-cemented horizons, when paired with laboratory synthesis of greenalite, suggests Fe(II)-rich and very low oxygen conditions were required to produce the earliest-forming minerals constituting iron formations (Tosca et al. 2016; Jiang and Tosca 2019; Hinz et al. 2021). These discoveries therefore represent a challenge to the longstanding model of a primary iron-oxide pathway of iron formation genesis where ferrous iron oxidizes and precipitates via interaction with oxygen, light, and/or microorganisms (Konhauser et al. 2017). Indeed, a new model of iron formation genesis has emerged wherein Fe(II) and silica interact abiotically to form iron silicates, providing an alternative iron formation deposition potentially independent of biologically-mediated processes (Rasmussen et al. 2021).

Previous studies evaluating mineralogy in silica-cemented horizons have generally focused on >2.5 Ga, pre-GOE iron formation (Beukes 1980, Rasmussen et al. 2014, 2015, 2017; Sheppard et al. 2017; Lantink et al. 2018; Tosca et al. 2019; Muhling and Rasmussen 2020), while fewer studies focus on the identification of mineral relationships in silica-cemented layers of Paleoproterozoic iron formations deposited following the GOE (Figure 1A-B). Intriguingly, multiple mineralogical studies of post-GOE iron formation note texturally early greenalite (French 1968, 1973; Floran and Papike 1975, 1978; Simonson 1987), and the presence of fine-grained Fe-Al-silicates (Rasmussen and Muhling 2020; Wacey et al. 2021). However, few studies have conducted in-depth examinations of iron silicate minerals in silica-cemented horizons in post-GOE iron formations (Rasmussen and Muhling 2020). Mineralogical studies of post-GOE iron formation are especially critical because the initial rise in oxygen may have been

73 followed by decreasing oxygen in the Paleoproterozoic (Figure 1B; Planavsky et al. 2012; Kipp
74 et al. 2017), which would impact the development and evolution of multi-cellular life.
75 Additionally, careful mineralogical studies–when performed within a well-defined
76 sedimentological and stratigraphic framework–may illuminate whether early oxygenation
77 occurred in only shallow water or extended into deeper water during the mid-Proterozoic (Figure
78 1C), a long-studied and debated topic. Deciphering the origin and evolution of complex mixed
79 valence iron silicate minerals may help to better constrain the persistence of reduced iron in deep
80 water, which in turn links directly to the location of the oxygen boundary in the post-GOE water
81 column.

82 Focusing on silica-cemented intervals as preservation windows into early forming
83 mineral phases in the ocean after the rise in atmospheric oxygen, we observed the textural
84 relationships and measured the chemical compositions of several different iron mineral phases in
85 the post-GOE, ~1.9 Ga Biwabik Iron Formation. We applied a complimentary suite of methods
86 to observe these iron minerals, including detailed petrography, scanning electron microscope
87 (SEM) equipped with energy dispersive X-ray spectroscopy (EDS), electron probe microanalysis
88 (EPMA) equipped with wavelength-dispersive spectroscopy (WDS), and Raman Spectroscopy.
89 Pairing textural relationships with mineral compositional data, we identified unit-specific
90 paragenetic sequences with texturally early iron silicates and associated diagenetic mineral
91 transformations. The goals of the present study include: (1) to assess preservation potential of
92 minerals within silica-cemented horizons of the Biwabik Iron Formation, (2) identify and
93 analyze iron silicate minerals, and determine their relationships to surrounding phases, and (3)
94 determine diagenetic reactions involving iron silicates and other iron mineral phases.
95 Reconstructing mineral formation histories helps establish paragenetic sequences and associated

conditions of formation for each mineral set. Identifying the conditions of formation for the earliest forming minerals allows for potential redox interpretations at or near the sediment/water interface. Following such an approach, future studies evaluating Archean and Paleoproterozoic iron formations as paleoenvironmental archives can evaluate early mineral preservation in silicified horizons to reconstruct unit specific paragenetic sequences, which may help to resolve disparate interpretations of redox conditions after the initial rise in oxygen on Earth.

GEOLOGIC BACKGROUND

The ~1.9 Ga Biwabik Iron Formation of the Mesabi range is part of the Animikie Group, a Paleoproterozoic sedimentary sequence extending from central Minnesota to southeastern Ontario that includes the iron formation of the Cuyuna range to the south and the Gunflint Iron Formation to the north (Figure 2A, B). The Animikie Group is one of several Paleoproterozoic supracrustal chemical and clastic sedimentary successions deposited from ~2200 to ~1780 Ma in the present-day Lake Superior region (Ojakangas 2001). Deposition of Paleoproterozoic sedimentary sequences began as continental extension and ocean opening caused basins to develop and accumulate sediment unconformably on the southeastern margin of the Superior craton (Schulz and Cannon 2007). Following the end of Animikie Basin sedimentation near ~1780 Ma (Heaman and Easton 2005), the later intrusion of the mafic Duluth Complex at ~1100 Ma isolated the likely-continuous Mesabi and Gunflint ranges of the Animikie Group, separating the two ranges with ~100km of plutonic, volcanic, and sedimentary rocks of the Midcontinent Rift System (Ojakangas 2001; Jirsa et al. 2008; Figure 2A, B). Iron formation proximal to but not removed by the Duluth Complex intrusion experienced contact metamorphism, though most of the iron formation including the drill core sample locations remain sub-greenschist facies

(Figure 2A, French 1968; Frost et al. 2007). Today, the Mesabi and Gunflint ranges dip southeast at ~10-20 degrees (Ojakangas et al. 2011).

In Minnesota, the Animikie group consists of the Pokegama Formation, the Biwabik Iron Formation, and the Virginia Formation (Figure 2C). The lowermost stratigraphic member, the Pokegama Formation, is a <50-meter siliciclastic unit composed of quartzite, argillite, and siltstone (Figure 2C). Radiometric Rb/Sr and Pb/Pb age dating of underlying dike swarms and cross-cutting quartz veins constrains Pokegama Formation deposition between 2125 ± 45 Ma and 1930 ± 25 Ma, respectively (Southwick and Day 1983; Hemming et al. 1990). During this depositional interval, paleo-environment interpretations based on observed bimodal cross-bedding sedimentary structures suggest deposition to be a near shore, tidally influenced shallow marine setting (Ojakangas 1983). Overlying the Pokegama formation is the Biwabik Iron Formation, a <225 m-thick chemical sedimentary unit whose inferred age of deposition comes from a single ash bed in the correlative upper Gunflint Iron formation dated at 1878.3 ± 1.3 Ma (Fralick et al. 2002), paired with the observation of the ~1850 Ma Sudbury Impact unit in the uppermost sections of the drill cores. The Biwabik Iron Formation is predominantly composed of authigenic iron minerals and chert. A low ~1% average Al_2O_3 composition (Morey 1992), coupled with the lack of visible terrestrial material in most drill core samples and thin sections indicates chemical sedimentation of the Biwabik Iron Formation occurred in a sediment-starved marine setting (Ojakangas 2001). However, some fine-grained beds have upwards of ~5% Al_2O_3 content (Morey 1992), and may contain terrestrial-sourced material too small to identify petrographically. Several thin sub-member horizons including the Basal Red and the Intermediate Slate contain significant terrestrial sediment (Figure 2C). Based on the gradational nature of the contact, the Basal Red likely represents a conformable transition from siliciclastic

142 sedimentation of the Pokegama to chemical sedimentation of the Biwabik (Severson et al. 2009).
143 Finally, directly overlying the Biwabik is the Virginia Formation, a siliciclastic sedimentary
144 sequence composed primarily of alternating greywackes, siltstones, and argillites. Alternating
145 bimodal grain sizes between beds and upwards coarsening packages suggest the Virginia
146 Formation was largely deposited as turbidite sequences (Lucente and Morey 1983). Rare ash
147 beds provide age constraints for the Virginia Formation at 1832 ± 3 Ma (Addison et al. 2005).
148 Overall, the three formations of the Animikie basin share similar lithologies and stratigraphic
149 packaging patterns with other iron formation-containing late Paleoproterozoic regional
150 sedimentary sequences (e.g., Akin et al. 2013; Eyster et al. 2021).
151 The Biwabik Iron Formation subdivides into four informal, texture-based members,
152 known as the Lower Cherty, Lower Slaty, Upper Cherty, and Upper Slaty. The descriptors
153 “cherty" and “slaty" are mining terms based on gross-scale architecture and correlation between
154 mine sites (Wolff 1917) and do not refer to the overall composition, cleavage, or metamorphic
155 grade (Ojakangas 2011). Within cherty members, alternating >1-5 cm beds of silica-cemented
156 (Figure 3A, B) and non-silica-cemented granules make up the primary sedimentary texture
157 (Severson et al. 2009). Granules are typically sand-sized and resemble arenitic textures in
158 siliciclastic sedimentary rocks (Simonson 1987). In the Upper and Lower Slaty members, beds
159 are typically thinner (<1cm) and composed of silt to clay-sized material instead of granules
160 (Figure 3C, D). However, rare beds composed of silt to clay-sized material and lacking silica
161 cement can contain granules. In this study, samples that possess quartz, chert, or chalcedony
162 cement will be referred to as “silica-cemented horizons" and layers that lack silica cement and
163 contain a predominant (but not exclusive) grain size of silt and/or clay will be termed “banded
164 horizons.” Both silica-cemented horizons and banded horizons can contain granules within this

nomenclature; however, silica-cemented horizons always contain granules, whereas banded horizons more commonly lack granules, and are defined by a lack of silica cement. Throughout Biwabik stratigraphy, silica-cemented horizons appear as either (1) continuous ~5mm - 1 cm tabular beds, or (2) as ovoid nodules where laminae above and below deform around the nodule indicating formation pre-compaction (Figure 3A-D).

METHODS

Sample Selection

Representative samples from each Biwabik Iron Formation member were collected from drill cores LWD-99-01 and LWD-99-02 at the Department of Natural Resources Drill Core Library in Hibbing, Minnesota. Drill cores LWD-99-01 and LWD-99-02 were selected as they represent the thickest part of the Biwabik Iron Formation and contain abundant material from all four members (Figure 2B, C; Severson et al. 2009). Sixty-eight samples were selected from both drill cores spanning Biwabik Iron Formation stratigraphy as well as portions of the underlying Pokegama and the overlying Virginia Formation (Figure 2C, gray circles). Finding and collecting silica-cemented samples involved searching for gray-to white-colored silica-cemented features in drill core, primarily in the form of nodules or tabular horizons (e.g., Figure 3A-D). To compare mineralogy between different horizons, all 68 samples were made into polished thin sections, with subsets specifically focused on encompassing both silica-cemented and banded horizons in single thin sections for data comparison.

Optical Microscopy

Mineral identification was conducted using a Nikon SMZ1270/800N large-field stereoscope and a Nikon Eclipse LV100N POL transmitted light (TL) microscope equipped with reflected light capabilities. Mineral phases were initially identified using respective diagnostic features in plane polarized (PPL) and cross-polarized light (XPL), with reflected light used for identifying mineral phases that appear opaque in transmitted light including Fe-oxides and sulfides. In addition to initial mineral identification, the following textural data was collected: (1) cross-cutting relationships between mineral phases and granule/cement contacts (Tables 1, 2); (2) granular textures including shape and internal granule structures (Supplementary Table S1).

Scanning Electron Microscopy

Following detailed petrographic characterization, a subset of samples were imaged and analyzed using Scanning Electron Microscopy to: (1) observe textural relationships between mineral phases at higher resolution, (2) establish/ test cross-cutting relationships identified using petrography, and (3) confirm identification of silicate mineral phases. Backscattered electron (BSE) images were collected with a JEOL JSM-6490LV SEM instrument equipped with an Energy Dispersive Spectroscopy (EDS) detector at the University of Minnesota Duluth Research Instrumentation Laboratory. Before SEM analysis, thin sections were coated with ~15 $\pm$5 nm of carbon using a LADD Vacuum Evaporator. Qualitative chemical compositions of mineral phases were measured with the EDS detector. Beam width for spot analyses varied between sessions but were typically ~5-100 μm wide to avoid analyzing multiple mineral phases per analysis. Spot analyses were operated at 10-15 kV with a ~70 second dwell-time. For select fine-grained samples, EDS element maps were collected to display distributions of Fe, Al, Mg, and Si in minerals too small for both EDS and WDS spot analyses (i.e., < than 3 μm). Element maps were

collected across a ~200 by 200 μm area at 15 kV, with a map dwell time of 100 μs and a total run time of 92 minutes. Element maps of Fe and Si were edited into a composite element map using ImageJ software (Schneider et al. 2012).

Electron Probe Microanalysis

After mineral phases were identified via optical microscopy and EDS, fourteen samples were selected for quantitative mineral analysis by EPMA (Table 1). Minerals analyzed come from samples that span all four members of the Biwabik and include iron silicates and carbonates both inside and outside of granules, as well as from non-granular textures (Table 1). This EPMA data was collected using a CAMECA SXFive field emission (SN944) electron microprobe located at the University of Wisconsin-Madison. Element concentrations were measured for specific mineral phases using a WDS detectors for X-rays generated from spot analysis. Elements for iron silicates were measured with the following mineral standards: Na and Al in jadeite, Mg, Al, Si, and Ca in hornblende, K in K-feldspar, Fe in hematite, Mn in Mn-olivine, and O in clinochlore. For measuring elements in carbonates, the following standards were used: Ca and Mg in dolomite, Fe in siderite, and Mn in rhodochrosite. Notably, O was measured in silicates, but not in carbonates. Spot analyses were conducted at 15kV using a 20 nA electron beam current. The X-rays were recorded for 10 s on the characteristic X-Ray peak and for 5 s on the backgrounds on each side of the peak. Spot size was adjusted, from 3 to 20 μm, to prevent beam damage of the analyzed material, especially for carbonates, and to prevent additional mineral phases from being measured during spot analyses, with beam width smaller than the mineral being analyzed. Minerals with sub-μm crystals were also measured when they occurred in monomineralic aggregates >3 μm, such as in greenalite or chamosite-bearing granules.

Verification of whether two different mineral varieties were measured in a single analysis included checking for visual differences in BSE imaging and for variability in chemical composition totals between different spot analyses in the same sample. Both of these measurement types found minimal examples of two or more different sub-μm mineral phases. Chemical compositions from WDS spot analyses were measured, matrix corrected using the PAP φ(ρz) correction (Pouchou and Pichoir 1991) and the MAC30 mass absorption coefficients (Heinrich 1987) as implemented in the Probe for EPMA software (Donovan et al. 2021), and reported as weight percent (wt%) oxide totals (Table 3). Data containing error range for WDS point analyses and point analysis locations can be found in the Supplementary Table S2. A cut-off of <97-101 wt% total was used when selecting spot analyses for calculating carbonate, minnesotaite, and stilpnomelane mineral formulas. Spot analyses with wt% oxide totals from 95-101% were used when calculating greenalite and chamosite mineral formulas. Lower oxide totals were used for greenalite and chamosite mineral formulas since these phases had lower average totals as they are hydrated phases. The lower totals were likely caused by the sub-μm mineral habits and difficulty measuring water (in the form of OH). Cation totals from mineral formulas were then plotted on ternary diagrams (Klein 2005) to compare mineral compositions from this study with the minerals in other iron formations or Fe-rich sedimentary rocks.

Raman Spectroscopy and Hyperspectral Maps

Raman spectra were acquired on ~1 μm target spots using a Horiba XploRA PLUS Raman spectrometer coupled to an Olympus BX41 microscope. We used a 532 nm laser excitation source (~1 mW), focused through a 100X objective lens with a grating of 1200 lines/mm (750 nm) and a 100 μm confocal pinhole to optimize spatial and spectral resolution.

The spectrometer was calibrated prior to analysis using a Si reference (peak at 520 cm^{-1}) and spectra were collected on a TE deep-air cooled -60 ºC CCD detector. We corrected spectral data for instrumental artifacts and subtracted baselines when needed using a polynomial fitting algorithm in the Horiba LabSpec 6 software. We also applied a smoothing function to produce an average of 5-10 adjacent points to remove background noise.

Hyperspectral maps of target areas were additionally produced to reveal complex mineral interactions observed in the samples. We produced these maps by rastering the microscope stage across a target region to generate spectra at each pixel. The hyperspectral dataset was fit by finding spectral endmembers within the map and applying a multicomponent Classical Least Squares fitting of endmembers to each pixel within the LabSpec 6 software. This quantitative analysis yielded a 'score' that we used to produce a color map showing the dominant phase at each pixel. Each endmember was matched to a known standard, either from internal lab collection or using the RRUFF public Raman database (Lafuente et al. 2015).

RESULTS

Within the Biwabik Iron Formation, the following minerals were identified via optical microscopy, SEM with EDS, EPMA with WDS, and Raman Spectroscopy: quartz, iron silicates (greenalite, chamosite, minnesotaite, stilpnomelane), carbonates (siderite, ankerite-dolomite, calcite) and iron oxides (hematite, magnetite). Results will be presented in two sections divided into focusing on the iron silicate mineralogy and then briefly describing the carbonate and iron oxide mineralogy. Textural attributes such as grain shape, morphology and internal textures were found to be closely related to specific mineral phases and are discussed in each respective

mineral section. Textural and mineral data is reported in Tables 1-3 and Supplementary Table S1. Mineral formulae are reported in Table 3 and Supplementary Table S2.

Iron silicate mineralogy

Chamosite. Chamosite, an Fe-rich chlorite [$(Fe,Al)_6(Si,Al)_4O_{10}(OH)_8$], occurs in granules as aggregates of sub-μm crystals. Chamosite mineral composition was measured from granules in three samples, MIR-19-12, MIR-19-15, and MIR-17-18 (Figure 4A, square symbols). Granules in MIR-19-12 and MIR-19-15 were located in and near banded horizons and in adjacent silica-cemented horizons (Figure 5A, sample MIR-19-12; Figure 5B -C, sample MIR-19-15), while chamosite mineral compositions in MIR-17-18 were collected within a banded horizon. Chamosite mineral data from all three samples range from 31-40 wt% FeO, 24-30 wt% SiO_2, 2-17 wt% Al_2O_3, and 6-14 wt% MgO (Figure 4A, Table 3, and Supplementary Table S2). No discernible differences in composition are noted between chamosite granules within the same sample. Chamosite contains significantly more Al_2O_3 relative to greenalite, minnesotaite, and stilpnomelane from this study (Table 3 and Supplementary Table S2).

Chamosite-bearing granules are mostly distributed within banded horizons or in silica-cemented horizons adjacent to banded horizons (Figure 5A-C). An example of this distribution can be seen in Figure 5A, where chamosite granules occur along the margins of a chert nodule (zone 1; Figure 5A) but decrease in density from the center of the nodule (zone 2, Figure 5A). In zone 2, chamosite is present as finely disseminated crystals, but granules are predominately composed of microcrystalline quartz. No chamosite was identified outside of granule boundaries as cement, although very fine-grained (<1 μm) chamosite is present in banded horizons (zone 3, Figure 5A, B). Texturally, chamosite is sometimes crosscut by stilpnomelane (Figure 5D),

carbonates, hematite, and/or magnetite. Notably, chamosite was not observed alongside greenalite within the same local mesobands or horizons.

Stilpnomelane. The Fe-silicate stilpnomelane [$(Fe,Mg,Al)_{2.7}(Si,Al)_4(O,OH)_{12} \bullet nH_2O$ with traces of K, Na, Ca; Klein 2005] forms ~3 -100 μm long subhedral-euhedral acicular or bladed crystals (Figure 5D). Stilpnomelane mineral compositions were measured from two banded horizon samples (MIR-19-3.5 and MIR-U-08; Figure 4B) and one silica-cemented sample (MIR-17-16; Figure 4B). Mineral compositions for stilpnomelane in sample MIR-17-16 were measured from crystals within a chert intraclast with no adjacent banded horizon (Duncanson 2020). All three stilpnomelane samples possess relatively comparable values of 43-49 wt% SiO_2, 3- 5 wt% Al_2O_3, and low but appreciable levels of 1- 2 wt% K_2O and ~0.5 wt% Na_2O (Table 1; Supplementary Table S2). Stilpnomelane from banded-horizons (MIR-19-3.5 and MIR-U-08; Figure 4B) contained lower Fe and higher Mg contents (25- 26 wt% FeO, 11-13 wt% MgO; Figure 4B, dark green/red diamond symbols) compared to stilpnomelane from silica-cemented horizons (34 wt% FeO, 3 wt% MgO; Figure 4B, light green diamond symbols). Stilpnomelane composition from the present study overlap with respect to Fe-Mg-Al concentrations measured in stilpnomelane from other iron formations (Figure 4A, B shaded gray region; Gole 1980 and Klein 2005).

Texturally, stilpnomelane distribution is highest within banded horizons, though it occurs as an internal granule phase as well as an intergranular cement among silica-cemented horizons as well. Stilpnomelane crystals commonly crosscut chamosite (Figure 5D) and greenalite. Stilpnomelane is always crosscut by magnetite and coarse $\geq$5 μm hematite crystals when these minerals are present, and sometimes crosscut by large, euhedral carbonate crystals.

Minnesotaite. The Fe-rich talc endmember minnesotaite [$Fe_3Si_4O_{10}(OH)_2$] most commonly forms bundles of ~5-50 μm long subhedral-euhedral acicular crystals resembling "felty masses" (Floran and Papike 1975). Minnesotaite mineral compositions were collected from intergranular and interstitial crystals in six samples (MIR-19-3.5, MIR-U-08, MIR-19-05, MIR-L-07, MIR-U-10, MIR-17-13; Figure 4C). Point analyses were collected for individual minnesotaite crystals or from homogenous minnesotaite crystal masses (Figure 6 A-F, Figure 7A-H). Raman spectroscopy analyses on three samples (MIR-L-07, MIR-U-10, MIR-17-13) additionally confirmed the identification of minnesotaite (Figure 7H).

Texturally, minnesotaite crystals crosscut sedimentary textures including granule-cement boundaries and non-compaction fractures within chert and greenalite granules (Figure 6A-D; Figure 7C-G). Minnesotaite commonly crosscuts greenalite and/or occurs as a first-generation cement phase associated with greenalite granules (Figure 6B, Figure 7D, G). In addition to occurring in direct association with greenalite, minnesotaite is also present as the only internal phases in some granules (Figure 6C, D). In these instances, minnesotaite occurs internal in the granule, and as a first-generation cement (Figure 6D). In two samples (MIR-19-3.5 and MIR-U-08) both stilpnomelane and minnesotaite mineral compositions were measured (Figure 4B, C). In sample MIR-19-3.5 (Figure 6E-G), minnesotaite granules are preserved inside the silica-cemented horizon (Figure 6E, F) and stilpnomelane granules are preserved at the margin of the silica-cemented horizon (Figure 6E, G). In this sample, stilpnomelane crosscuts minnesotaite (Figure 6G), but generally throughout the section, minnesotaite alternates cross-cutting relationships with both stilpnomelane and carbonate crystals indicating multiple generations of regrowth and/or recrystallization of those phases. Minnesotaite is always crosscut by euhedral magnetite when present (Figure 6F, G).

Minnesotaite mineral compositions (Figure 4C) in samples MIR-L-07 (Figure 6A, B; Figure 7F,G), MIR-U-10 (Figure 7A-E), and MIR-17-13 (Figure 8A-F) come from silica-cemented horizons and show a direct textural relationship with greenalite (e.g., Figure 6B), while minnesotaite in samples MIR-19-05 (Figure 6C-D), MIR-U-08, and MIR-19-3.5 (Figure 6E-G) were measured from silica-cemented horizons that lack greenalite (Figure 6C-G). Minnesotaite bundles that occur within granules compared to those that occur as interstitial cements show no difference in composition in the same sample. However, a large compositional difference was measured for FeO and MgO content between minnesotaite texturally associated with greenalite (e.g. sample MIR-L-07; Figure 4C) compared to minnesotaite associated with stilpnomelane (e.g. sample MIR-19-3.5; Figure 4C). Minnesotaite in stilpnomelane-rich samples MIR-19-3.5 (Figure 6E and F) and MIR-U-08 have similar ~17 wt% FeO and ~20 wt% MgO compositions (Figure 4C; Table 3, Supplementary Table S2), whereas minnesotaite from greenalite-bearing samples MIR-L-07, MIR-U-10, MIR-19-05, and MIR-17-13 have higher average 33-42 wt% FeO and lower 2-7 wt% MgO (Figure 4C). Additionally, Raman point spectra confirm the presence of minnesotaite in these samples despite its FeO content measuring higher than expected. Consequently, the MgO and FeO content of stilpnomelane-associated minnesotaite (Figure 6E and F) resembles the talc-minnesotaite series compositions observed in other iron formations (Klein 2005), whereas minnesotaite alongside greenalite and/or lacking stilpnomelane contain enough FeO to plot outside of Klein (2005) mineral series (Figure 4C). Similar Fe-rich minnesotaite is noted in the Gunflint Iron Formation (Floran and Papike 1975).

Greenalite. Greenalite was identified in several Biwabik samples through a combination of mineral composition and Raman spectroscopy. Greenalite, the iron endmember mineral from

the serpentine clay group [ideal formula: $Fe_3Si_2O_5(OH)_4$)], is present among silica-cemented horizons in two distinct habits: (1) as aggregates of sub-µm crystals which constitute whole granules (Figure 7A-G), resembling greenalite granules previously noted in the Biwabik and Gunflint Iron Formation (Leith 1903; French 1968, 1973; Floran and Papike 1975); and (2) as sub-µm disseminated inclusions within chert granules giving an overall 'dusty' appearance (Figure 8G-I), similar to greenalite-bearing chert in banded iron formations (Rasmussen et al. 2017; Muhling and Rasmussen, 2020). As previously described, some granules contain a mixture of fine-grained, disseminated greenalite and minnesotaite (Figure 8A, B) where minnesotaite occurs inside granules (Figure 6F, 8F) and as an intergranular, first-generation cement (Figure 8C). Other samples contain granules composed entirely of greenalite, and minnesotaite only occurs as intergranular cement nucleating off the exterior boundaries of granules (Figure 8D – F) or nucleating from granules into quartz-filled non-compaction fractures (ncf) inside individual granules (Figure 7G). Non-compaction fractures (ncf; Figure 7F, G) are common in greenalite and chert granules throughout the drill core. Notably, greenalite is only found within granules and not as an intergranular cement phase among the surrounding quartz cement. Aggregates of greenalite appear dark green to opaque in transmitted light. Both the disseminated and aggregate forms of greenalite were only found within silica-cemented horizons, and were not identified within banded horizons, though the possibility exists of unidentified fine-grained (sub-µm) greenalite disseminated within banded horizons.

Mineral composition data (Figure 4D; 7H) was collected from two samples (MIR-U-10; Figure 7A - F; MIR-L-07; Figure 7G, H) containing granules with aggregates of sub-µm crystals large enough (> 3µm) for microprobe point analysis. Samples MIR-L-07 and MIR-U-10 range in composition from ~45-51 wt% FeO, 33-34 wt% SiO_2, and contain appreciable ~3-6 wt% MgO

content (Figure 4D; Table 3, Supplementary Table S2). Minnesotaite cement was also measured from three samples containing greenalite granules (Figure 4C, and Figure 7E, H). The chemical compositions of greenalite in both samples resemble greenalite in other iron formations (Figure 4D, greenalite field); this includes a minor excess of Si relative to the ideal 4.00 Si in greenalite, with an average 4.13 and 4.05 Si formula ions in MIR-L07 and MIR-U-10. respectively (Table 3 and Supplementary Table S2). Excess Si ions are noted for microprobe measurements of greenalite in other iron formations, likely linked to sub-µm quartz impurities present within aggregates of greenalite (Floran and Papike 1975; Gole 1980). In some instances, there appeared to be a mixture of two phases present near noncompaction fractures inside granules (Figure 7E), which could be due to sub-µm quartz impurities and/or excess Si (Gole 1980). Disseminated greenalite inclusions within chert granules were too small (< 1 µm) for WDS spot analysis and were instead measured semi-quantitatively with EDS spectra (Figure 8G-I). Based on their high Fe, Si, and O peaks, with smaller Mg peaks, these inclusions were identified as greenalite, similar to other iron formation studies (Figure 8G-I; Muhling and Rasmussen 2020).

Carbonate and iron oxide mineralogy

Carbonate minerals are most commonly present as large (~0.1 - 5mm) subhedral-euhedral crystals (Figure 9A, B). Texturally, large carbonate crystals occur in the highest density within banded horizons and directly adjacent to banded horizons. Within silica-cemented horizons, carbonates typically transect granule-cement contacts (e.g., Figure 9A) and crosscut most iron silicate minerals, although because there are multiple generations of carbonate crystals, this phase can show both earlier and later cross-cutting relationships with minnesotaite and stilpnomelane crystals (Figure 9B). In addition to occurring proximal to or as banded layers

(Figure 7A, bands), carbonate crystals also appear in chert intraclasts (Figure 9C, D). Compositionally, carbonate crystals typically have varying FeO, MgO, and CaO content resulting in an array of ferroan dolomite-ankerite series to siderite compositions (Figure S1). This compositional variation is noted between the rims and cores of single crystals as well as between carbonate minerals from different samples and is typical of ferroan dolomite-ankerite series carbonates within other iron formations (Krapež et al 2003; Flügel and Munnecke, 2010). Carbonate crystals are consistently crosscut by magnetite (Figure 9E) and coarse hematite crystals (Figure 9F, G). Preliminary results of Biwabik carbonate textures and additional context for compositional data are presented in the M.S. thesis by S. Duncanson (Duncanson, 2020) and are the subject of a separate study.

Magnetite and hematite are the most common iron oxides observed throughout the Biwabik Iron Formation. Magnetite (Fe_3O_4) forms ~10-20 μm euhedral crystals (Figure 9E-G). It crosscuts all other minerals phases when present, including coarse hematite (Figure 9F, G). Hematite (Fe_2O_3) crystals range from fine grained (<1-5 μm; Figure 9H) to coarse (≥5 μm) euhedral laths (Figure 9E-G). Both fine- and coarse-crystal sizes are found within chert granules, as cement in both silica cemented and banded horizons as well as uniquely forming concentric layers of chert-hematite ooids in the Basal Red and Upper Cherty units (Figure 2), as well as in stromatolitic horizons of the Lower Cherty (Planavsky et al. 2009; Severson et al. 2009). Coarser crystal hematite laths most typically crosscut Fe-silicate and carbonate minerals, granule-cement boundaries, and quartz cement between granules (Figure 9F, G). Fine, nanoscale hematite constitutes layers which coat grains (Figure 9H). Importantly, such examples of fine-grained hematite are not seen alongside greenalite and minnesotaite, and instead are present in samples with abundant microquartz (Figure 9H). Therefore, although there may be other stratigraphic

intervals where iron oxides are primary, hematite mineralizing within the examined Fe-silicate-rich samples all appears secondary.

DISCUSSION

In the following discussion, we suggest interpretations of primary and secondary relationships of iron minerals, propose iron silicate diagenetic reactions using mineral compositions and textural relationships, and then develop a paragenetic sequence model based on textural observations in the Biwabik Iron Formation. Below, we describe cross-cutting relationships and compositional data for diagenetic and texturally early minerals observed in silica-cemented horizons and compare these features to adjacent banded horizons to inform potential mineral reactions and identify possible precursor mineral phases. We define texturally early minerals following a modified version of the "primary mineral" classification for iron formation mineralogy described in Laberge (1964), including (1) a very fine grain size (combined with the information that samples only experienced low temperature and pressure conditions throughout their history, indicating that grain size reduction during metamorphism is unlikely); (2) a uniform size distribution; (3) a particulate or granular texture, and (4) a close association with sedimentary features such as bedding. In the present study, minerals that meet all four Laberge (1964) criteria are termed 'texturally early' to recognize that they may still form after other minerals. We also acknowledge that geochemical exchange may have occurred during the transformation from amorphous phases to crystalline minerals. Furthermore, we observed that some fine-grained minerals cross-cut other minerals and thus likely form a sequence of identifiable mineral reactions that occurred during early diagenesis. In addition, we add the criteria that texturally early minerals should occur within early chert granules and do not transect

462 granule-cement contacts or occur as intergranular cements. Minerals formed outside of granules
463 but within the same horizon are interpreted based on their textual relationship to granules, and as
464 a result, are identified as occurring after granule formation.

465 The focus of the present study is the documentation of mineral relationships, specifically
466 those preserved in silicified horizons of the Biwabik Iron Formation. The discussion centers on
467 interpretations of observed textures and compositions in such horizons. In the following section,
468 we outline diagenetic mineral relationships preserved in silicified regions of the Biwabik Iron
469 Formation, following our mineralogical identifications and interpretations by interpretations of
470 texturally early phases, with a focus on deciphering the origin of iron silicate phases preserved in
471 the Biwabik Iron Formation.

472

473 **Texturally early minerals in the Biwabik Iron Formation**

474 Textural relationships between mineral phases within silica-cemented horizons preserve
475 clear evidence of their relative timing of precipitation, providing insights into possible precursor
476 sediment composition(s). Through the previously described framework, we identified texturally
477 early minerals of the Biwabik Iron Formation to include microcrystalline quartz (in the form of
478 chert), greenalite, and chamosite, and fine-grained hematite. Minerals identified as having a clear
479 secondary, diagenetic origin include stilpnomelane, minnesotaite, euhedral carbonate crystals,
480 and magnetite. Some fine-grained hematite examples show evidence for texturally early
481 formation (Figure 9H), though most commonly, these phases occur as clear diagenetic minerals
482 that cross-cut earlier phases (e.g., Figure 9A, F, G). Examples of texturally early fine-grained
483 hematite include crystals that are distributed as sub-μm crystals within stromatolite layers or
484 coated chert grains in restricted horizons (e.g., Basal Red unit, Figure 2; Figure 9H).

Microcrystalline quartz is a pervasive early cement in silicified horizons, commonly crosscut by later minnesotaite and stilpnomelane cement, as well as euhedral carbonate and magnetite. The formation of chert nodules surrounded by differentially compacted banded layers (e.g., Fig. 3D) supports microcrystalline quartz being an early phase in the Biwabik Iron Formation sediments. Chert granules commonly show non-compaction fractures (e.g., 8G, H) interpreted as dewatering fractures linked to dehydration of an initial hydrous silica-gel granule composition (Simonson 1987; Maliva et al., 2005). Initial hydrous silica may have been deposited via adsorption onto settling precursor sediment (Fisher and Knoll 2009; Konhauser et al. 2017; Rasmussen and Muhling 2020) and/or as a primary SiO_2 precipitate (Stefurak et al. 2014; 2015).

Greenalite does not cross-cut other mineral phases from this study, and is not observed filling non-compaction fractures, or as a cement phase, suggesting greenalite precipitation occurred prior to granule fracturing. Granules composed primarily of greenalite display dewatering fractures filled entirely with quartz cement (Figure 7B; 8G), suggesting greenalite precipitation concurrent with or prior to dewatering. If greenalite formation occurred after dewatering, then we would expect fractures to be filled with or crosscut by greenalite, similar to the minnesotaite that nucleates off granule surfaces into non-compaction fractures or surrounding granules as a first-generation cement in these samples (Figure 7G; 8C). Pairing these textural observations with greenalite mineral composition supports interpretations of iron silicates as texturally early phases.

Both greenalite within chert granules and greenalite aggregates from the Biwabik Iron Formation share similar compositional ranges (Figure 4D) and textural habits with greenalite from other iron formations (Floran and Papike 1975; Rasmussen et al. 2017, 2019; Johnson et al.

508 2018; Muhling and Rasmussen 2020). These prior studies suggest that greenalite compositions
509 most closely approximate the initial primary precipitate composition based on textural
510 observations. For example, dusty chert beds containing silica-cemented greenalite inclusions in
511 late Archean and early Proterozoic iron formation are interpreted to represent the precursor
512 sediment consisting of greenalite or a greenalite-like precursor phase (Muhling and Rasmussen
513 2020). Sub-μm greenalite in dusty chert granules of the Biwabik Iron Formation visually
514 resemble dusty chert beds as well as resembling "cloudy" chert granules containing a sub-μm
515 silicate phase in other late Paleoproterozoic granular iron formations (Simonson 1987). If
516 greenalite in the Biwabik Iron Formation closely approximates the precursor sediment
517 composition, then granules likely have a precursor composition with significant ferrous iron,
518 silica, and water, resembling a greenalite-like gel (Tosca et al. 2016, 2019; Hinz et al. 2021).
519 Alternatively, texturally early greenalite could mineralize after reduction of a precursor iron
520 (oxy)-hydroxide or similar phase (Robbins et al. 2019), though no direct textural relationships
521 were observed in samples to support or identify such reactions.

522 Fine-grained chamosite provides insight into precursor sediment composition as well,
523 though the distribution of chamosite granules within silica cement and its high aluminum content
524 suggest its likely precipitation during early diagenesis at the same time as or shortly after the
525 precipitation of chert and potentially other iron-bearing primary mineral phase(s). Unlike
526 greenalite, chamosite does not form ubiquitously within silica-cemented horizons, but instead
527 forms adjacent to or within banded horizons (Figure 5A-C). The limited spatial distribution of
528 chamosite granules is likely due to the high aluminum content of chamosite, with sufficient
529 aluminum most likely sourced from fine-grained terrestrial or volcanic-derived material within
530 banded horizons (Morey 1992). Due to the limited mobility of aluminum in pore fluids (Wintsch

and Kvale 1994), chamosite could be restricted to forming proximal to aluminum sources in the banded horizons, while silica and iron could derive from a precursor sediment phase within granules. An example of aluminum-dependent distribution can be seen in Figure 5A (zone 1) where green-colored chamosite granules are more abundant close to the banded horizon along the margins of the nodule while the center of the nodule contains light-toned granules composed primarily of chert (Figure 5A; zone 2).

Since chamosite is still fine-grained and crosscut by diagenetic mineral phases such as euhedral carbonate, we propose that the likely precursor phase for chamosite in the Biwabik was a hydrous iron-silica gel that reacted with local aluminum-bearing sediments, similar to the mechanism proposed by French (1973). Local aluminum, silica, and iron-rich precursor phases are suggested for chamosite formation in other iron-rich rocks (Klein 2005). Specific examples of local aluminum influence on chamosite formation include chamosite-bearing ooids in Ordovician ironstones, where sufficient silica, iron, and aluminum concentrations for chamosite precipitation were supplied by rapidly deteriorating volcanic ash (Sturesson et al. 2000) and chamosite wisps in the Gunflint Iron Formation, where chamosite is restricted to tuffaceous shale facies and interpreted to form from precursor volcanic shards (Floran and Papike 1975). Formation of chamosite from an amorphous iron hydroxide-silica precipitate in the presence of iron, aluminum, and magnesium can occur under low temperature reducing conditions (Harder 1978).

We recognized two types of hematite which we distinguished as early and secondary. Most typically, hematite forms >5 μm euhedral to subhedral crystals which transect granule-cement contacts, indicating formation following granule deposition and silica cementation (Figure 9F, G). Therefore, these large hematite crystals which crosscut texturally early minerals

554 in the Biwabik Iron Formation or form outside of granules in association with cement are
555 classified as secondary. In contrast, we observed in the Basal Red and Upper Cherty stratigraphic
556 intervals (Figure 2C) examples of sub-μm scale hematite within layers coating grains, which
557 were labeled as texturally early. Other examples of fine-grained hematite in the Gunflint and
558 other iron formations have been found to cross-cut Fe-silicates, suggesting the phase may form
559 secondarily while remaining fine-grained (Rasmussen et al. 2016; Rasmussen and Muhling
560 2020). Additionally, because the water column was likely stratified with respect to oxygen and
561 iron concentrations across the Proterozoic, it is possible and very likely that shallow water and
562 deeper water units possess different sets of texturally early phases that relate back to the position
563 of the oxygenated boundary in the water column (commonly called the redoxcline). As a result
564 of this chemistry, in the oxygenated part of the water column, hematite may form as an early
565 mineral phase from oxidized waters, which may explain why observations of fine-grained
566 hematite in the Biwabik Iron Formation are limited to stromatolitic horizons, coated grains, or
567 associated thin laminae.
568
569 **Secondary iron silicate mineral compositions**
570 In addition to preserving texturally early greenalite and chamosite, silica-cemented
571 horizons also preserve minnesotaite and stilpnomelane assemblages that crosscut texturally early
572 phases and granule-cement boundaries. Euhedral to subhedral acicular minnesotaite and
573 stilpnomelane crystals (~50 μm or less) visibly cross-cut granule-cement boundaries and appear
574 as interstitial cement phases, and often cross-cut chamosite (Figure 5D) and greenalite (Figure
575 6B; 7G). Such textural relationships suggest minnesotaite and stilpnomelane form after granule
576 formation and both during and/or after silica cementation. However, the presence of

577 stilpnomelane inclusions within pebble-size chert intraclasts (Figure 9C, D) and not in the
578 surrounding granules or cement suggests stilpnomelane can form prior to erosion, transportation,
579 and redeposition of intrabasinal chert intraclasts. Transport and redeposition of stilpnomelane-
580 bearing chert intraclasts suggest stilpnomelane may be able to form close to the sediment-water
581 interface (Simonson 1987). This interpretation is in line with previous studies, where acicular
582 stilpnomelane and minnesotaite were classified as forming during early diagenesis in granular
583 iron formation (Dimroth and Chauvel 1973; Floran and Papike 1975) and banded iron formation
584 (Gole 1980; Pecoits et al. 2009). Minnesotaite and stilpnomelane likely form from secondary
585 reactions of texturally earlier iron silicates.

586 Minnesotaite is commonly observed cross-cutting greenalite granules and/or as a cement
587 (Figure 6D; Figure 8C-D) and likely forms as a reaction product of greenalite and chert (French
588 1973; Klein 2005). Compositionally, minnesotaite that crosscuts greenalite or forms cement
589 between greenalite granules is Fe-rich, resembling greenalite compositions within the same
590 sample (Figure 4C, D). We hypothesize that samples lacking greenalite but containing granules
591 that are predominantly composed of Fe-rich minnesotaite (Figure 4C; Figure 8A-C) may derive
592 from complete replacement of greenalite in diagenetic environment with abundant silica. This
593 mechanism is supported by our observations of granules in sample MIR-17-13 where Raman
594 spectroscopy showed greenalite-dominated granules with varying admixtures of minnesotaite
595 within the granules and minnesotaite-dominant cross-cutting cement and small veinlets (Figure
596 8D-F). Alternatively, Fe-rich minnesotaite may originate from reactions with other iron bearing
597 texturally early precursors such as hematite, siderite, or chamosite reacting with chert (Floran
598 and Papike 1978). However, no clear examples of hematite or chamosite being crosscut by

599 minnesotaite were observed in this study, whereas there were abundant observations of
600 minnesotaite cross-cutting greenalite.

601 Assuming greenalite or similar iron and silica-bearing phases are precursors for Fe-rich
602 minnesotaite, then minnesotaite with higher magnesium content may indicate a more Mg-rich
603 precursor phase and/or magnesium incorporation (or Fe loss) during diagenesis. Unlike the iron-
604 rich minnesotaite that is distributed solely within tabular silica-cemented horizons (Figure 6A),
605 granules containing Mg-rich minnesotaite (MIR-U-08 and MIR-19-3.5, Figure 4C) are in silica-
606 cemented nodules surrounded by fine-grained banded horizons (Figure 6E). Within these
607 nodules, minnesotaite granules located adjacent to the nodule margins are crosscut by additional
608 diagenetic mineral phases, including stilpnomelane (Figure 6G). These minnesotaite and
609 stilpnomelane crystals have similar chemical compositions, containing significantly higher
610 magnesium and lower iron concentrations than the same mineral phases in tabular silica-
611 cemented horizons (Figure 4B, 4C). In these samples, Mg-rich minnesotaite is found near banded
612 horizons and cross-cutting stilpnomelane, suggesting banded horizons and/or their precursory
613 sediment-pore fluid admixture, could be a potential magnesium source (Gole, 1980). The higher
614 abundance of cross-cutting diagenetic minerals like stilpnomelane along chert nodule margins
615 (Figure 3B) suggests a greater degree of diagenetic mineralization, perhaps driven by additional
616 exposure to diagenetic pore fluids within the surrounding banded horizon. Assuming Mg-rich
617 minnesotaite granules have the same iron and silica precursor phases as the Fe-rich minnesotaite
618 within tabular silica-cemented horizons, then diagenetic Mg-bearing pore fluids sourced from the
619 banded horizons could have altered the original iron and silica precursor phases. Pore fluid
620 interaction could have also driven a mineral reaction from minnesotaite to cross-cutting
621 stilpnomelane with a similar iron and magnesium composition, albeit with an additional influx of

622 aluminum. Stilpnomelane observations from the present study are in line with previous work on
623 Gunflint and Biwabik Iron Formation mineralogy, which also suggest stilpnomelane can form
624 from precursor minnesotaite (Floran and Papike 1975; McSwiggen and Morey 2008).

625 The observed distribution of stilpnomelane in samples MIR-U-08 and MIR-19-3.5
626 (Figure 5D; 6E, G) is common, where stilpnomelane typically crosscuts chamosite or
627 minnesotaite near banded horizons. The textural association of chamosite and stilpnomelane near
628 banded horizons (and significant concentrations of aluminum in both phases; Table 3, Figure 4A,
629 B) may point to a local aluminum source from adjacent (non-silica-cemented) bands for both
630 minerals. In addition, stilpnomelane contains significant magnesium, potassium, and sodium
631 concentrations relative to the other iron silicates in this study (Table 3), suggesting diagenetic
632 fluids capable of sourcing these elements likely played a key role in stilpnomelane formation as
633 well (Gole 1980). We therefore propose that stilpnomelane likely forms from precursor phases in
634 the Biwabik that can supply sufficient iron, aluminum, magnesium, and silica incorporating
635 additional potassium and sodium from fine-grained material in surrounding banded horizons
636 during mineralization. Previous Biwabik mineralogical studies proposing stilpnomelane
637 precursors include chlorite and quartz (French 1968) as well as volcanic and/or extrabasinal
638 siliciclastic material within banded horizons (French 1973). The source of aluminum for
639 stilpnomelane-rich units within iron formation of the Transvaal Supergroup are also attributed to
640 the input of volcanic material (Beukes and Klein 1990).
641

642 **Reversing diagenetic reactions to identify primary precipitates that link to seawater**

643 In both banded and silica-cemented horizons of the Biwabik Iron Formation, mineral
644 assemblages preserve a sequence of incomplete diagenetic reactions which allow the

development of paragenetic sequence sets. By pairing the relative order of formation between texturally early and secondary, diagenetic minerals with mineral compositions, we can identify the relative order of mineral precipitation and associated geochemical exchange. Reversing these geochemical reactions, we can potentially determine a set of potential precursor mineral compositions that may link back to seawater composition.

In this study, we found that horizons that lack silica cement show evidence for local geochemical exchange between pore fluids and hydrous iron and silica precursor sediments. Silicates adjacent to or among banded horizons incorporate more aluminum and/or magnesium (forming chamosite, stilpnomelane, and minnesotaite associated with stilpnomelane; Figure 4A-C). Silicates proximal to banded horizons are also crosscut by carbonate and iron oxide minerals more frequently than those within tabular silica-cemented horizons. In tabular silica-cemented horizons, the likely rapid encapsulation of precursor sediment immediately following deposition could reduce geochemical interaction with local terrestrially sourced sediment and/or oxidizing fluids to varying degrees.

Within tabular layers cemented by silica, we observe silicates with iron endmember compositions (Figure 4C, mns; Figure 4D, gre), and minerals that lack Al and Mg. This may be because silicified layers would have little to no interaction with diagenetic fluids and the surrounding sediment after cementation. Silicified layers may therefore present the best geochemical record of mineral interactions that occur at/ near the sediment-water interface. Using a holistic approach of putting together mineral compositions, cross-cutting relationships, and observed spatial distributions of phases within silica-cemented horizons, we interpret possible mineral reactions from the precursor sediment through diagenesis in silica-cemented and banded layers of iron formation and illustrate these with emphasis on iron silicates in Figure

668 10. We recognize the importance of oxide and carbonate phases in iron formation and their
669 potential link to seawater conditions as primary minerals in some settings. In this work, the
670 presence of texturally early oxides in some horizons of the Biwabik does not alter conclusions
671 regarding the importance of early silicates for the Biwabik Iron Formation. Instead, it highlights
672 the need for paired mineralogy and stratigraphy studies in order to detangle stratigraphic patterns
673 in mineral distributions, which is the focus of ongoing work in the region.

674 The earliest forming minerals identified in the Biwabik Iron Formation are most
675 commonly greenalite and chert within granular silica-cemented or banded horizons, and
676 hematite, which is confined to stromatolitic or ooidal horizons. Importantly, in samples that meet
677 the criteria to preserve texturally early phases, the two texturally early redox sensitive minerals
678 (greenalite, hematite) are not found in association with one another, but instead are found in
679 separate parts of the stratigraphy. The lack of a direct textural connection between the two
680 texturally early phases could support the presence of an oxygen gradient or redoxcline within the
681 basin (Akin et al. 2013) or may indicate the potential for partial oxidation of reduced phases
682 within the water column or at/near the sediment-water interface. Because the Biwabik Iron
683 Formation was deposited after the GOE and there is experimental support that mixed-valence
684 proto iron silicate phases readily form (Hinz et al. 2021), we suggest the primary precipitates in
685 the Biwabik Iron Formation were mixed Fe^{2+} and Fe^{3+} valence state, silica-rich gels ($Fe^{2+,3+}$-Si-
686 O-OH) (Figure 10A).

687 We also identify that silicification (both nodular, and tabular) occurs very early, likely at
688 the sediment water interface. To illustrate these two modes of silicification (nodular and tabular)
689 and account for the differences we see in post-depositional mineral assemblages of silicified
690 layers compared to non-silicified layers, we divide initial sediment deposition into three

scenarios in Figure 10A. In scenario 1 (left panel of Figure 10A), there is little to no silica added to the initial sediment (non-silicified). In scenarios 2 and 3 (the middle and right panels of Figure 10A), silica is added to the sediment (as H_4SiO_4) and is likely sourced from seawater, as seawater silica concentrations were high across the Paleoproterozoic prior to the evolution of silica-secreting organisms (Siever 1992). Additionally, we account for potential addition of terrigenous material and its effects on the composition of some diagenetic minerals in scenarios 1 and 2 based on the data from the present study.

Post-deposition (Figure 10B), there are different mineral sets and unique textural relationships preserved between phases for each scenario. With limited silicification in scenario 1, primary precipitates are susceptible to post-depositional changes, which could include redox reactions. If oxygenated fluid interacts with the sediment at any point, then primary reduced or mixed phases will oxidize (Figure 10B, reaction pathway B1; reaction 1). This type of oxidation could occur, for example, during sea level fall and subsequent intersection of reduced sediments with the oxygen boundary in the water column (e.g., Todd et al. 2019), or through later fluid migration along bedding planes or fractures at any time in the geologic history of the unit (Losh and Rague 2018). With the lack of silica cement, reactive minerals are likely to exchange cations, resulting in the formation of phases like stilpnomelane (Figure 10B; reaction pathway B1; reaction 2). Even with limited cementation during formation of chert nodules (Figure 10B; scenario 2) fluid flow and geochemical exchange may occur at the boundaries of silicified areas and banded (non-silica-cemented) layers. Here, aluminum sourced from terrigenous material may promote local formation of both chamosite and stilpnomelane at or near nodule boundaries (Figure 5A-C; Figure 10B; reaction pathway B2; reaction 5,6). Based on our observations, we propose that a geochemical gradient preserves the inner chert nodules, where in the center

(earliest precipitating) part of the chert nodule, granules composed of the precursor sediment mineralize to iron silicates and quartz (Figure 10B; reaction pathway B2). Only in scenario 3, where entire beds are silicified, do we see maximum preservation of reduced iron silicate phases such as greenalite (Figure 10B; reaction pathway B3; reactions 7, 8), along with a lack of textural and compositional evidence for local geochemical exchange. In all three scenarios, carbonate minerals, represented in Figure 10 as siderite, form after silicate minerals (Figure 10B, reactions 3, 9). Some carbonate crystals are observed forming prior to minnesotaite and stilpnomelane (Figure 5D, and Figure 9B), indicating some secondary iron silicates continue forming after carbonate formation, most carbonate minerals cross-cut silicate phases (Figure 9A). Magnetite crystals cross-cut carbonate and all other mineral phases (, Figure 6G; Figure 9E-F) and are the last forming mineral in all three scenarios (Figure 10B, reaction 4). The higher proportion of magnetite observed in banded horizons relative to silica-cemented ones further suggests increased local geochemical exchange between pore fluids and earlier forming reactive minerals, resulting in increased magnetite mineralization from precursor siderite (Figure 10B, reaction 4) and/or iron silicates (Figure 6D; Rasmussen and Muhling 2018). Overall, we therefore conclude that silicification links to the preservation of reactions that allow us to unravel diagenetic reactions and leads to the potential to identify primary precipitates that may link back to seawater chemistry at the time of formation.

IMPLICATIONS

Silica-cemented horizons in the Biwabik Iron Formation preserve Fe-rich silicate mineral assemblages and capture diagenetic reactions *in situ*. Because of this textural preservation, several inferences can be made regarding silica cementation and precursor sediment preservation

737 in the Biwabik, which may extend to other post-GOE iron formations and provide potential
738 insight into Paleoproterozoic seawater geochemistry. First and foremost, silica-cemented nodules
739 preserve diagenetic reactions between iron silicate phases at nodule margins, revealing the
740 effects of local geochemical exchange during diagenesis (Figure 10). Geochemical exchange
741 during early diagenetic reactions modifies the composition of primary phases, complicating
742 mineral composition-based precursor sediment interpretations. With the recent focus on early Fe-
743 silicates in iron formations as proxies for seawater composition and redox conditions (e.g.,
744 Rasmussen et al. 2017; 2021), future studies should continue to constrain iron silicate mineral
745 paragenesis using paired petrographic and geochemical approaches to identify effects of local
746 geochemical exchange.
747 In silicified layers of the Biwabik Iron Formation, we identified texturally early
748 greenalite that may represent the redox state of the precursor sediment, indicating primarily
749 anoxic conditions existed in some parts of the basin where sufficient ferrous iron and silica were
750 available for greenalite precipitation. Precipitation of a greenalite-like precursor sediment could
751 have been driven by an increase in seawater pH (Tosca et al. 2016; Rasmussen et al. 2017)
752 and/or a minor increase in available ferric iron that initiated iron silicate precipitation (Hinz et al.
753 2021). Though most hematite was observed to have mineralized after Fe-silicate phases when
754 present in the same sample, a few noteworthy samples from specific stratigraphic intervals
755 display hematite and chert as the earliest forming minerals (Basal Red and Upper Cherty, Figure
756 2) while lacking any texturally early iron silicates (e.g., Figure 9H). If these hematite samples
757 represent precursor sediment precipitation under suboxic to oxic conditions, then perhaps
758 precipitation of hematite and greenalite reflects mineral precipitation above and below a
759 redoxcline, respectively. Similar oxygen-stratified depositional settings are suggested for other

760 post-GOE Paleoproterozoic iron formation (Wilson et al. 2010; Akin et al. 2013; Pufahl et al.
761 2014). Since the Biwabik contains similar mineral assemblages as iron formations predating the
762 GOE, future studies should continue to explore relationships between texturally early mineral
763 phases and redox conditions of equilibrium assemblages. This approach - considering how
764 paragenetic mineral assemblages can vary throughout iron formation stratigraphy (e.g. Beukes
765 1980), could help to clarify interpretations of redox conditions near the sediment/water interface
766 for Precambrian iron formations where different proxies indicate disparate original oxidation
767 states inferred to represent the time of deposition.

768 More broadly, it may be useful in future mineralogical studies of iron formation to
769 consider textural relationships and mineral identification within silica-cemented horizons via
770 combined transmitted and reflected light microscopy, electron microscopy, and spectroscopy
771 techniques to gauge the effects of local geochemical exchange between bands during early
772 diagenesis. Since geochemical exchange can affect early-forming mineral compositions while
773 retaining primary mineral classification under the Laberge (1964) criteria, similar precaution
774 should be taken for geochemical consideration of putative primary mineralogy in other
775 Precambrian iron formations.

776

777 **ACKNOWLEDGEMENTS**

778 This work was funded by internal awards to L. Brengman from the University of Minnesota
779 Duluth, and student research grants awarded to S. Duncanson from the Geological Society of
780 America, and the Institute of Lake Superior Geology. We would like to specifically thank
781 undergraduate students Stephen Hanson, Anthony Wetzel, and Kendall Johnson for sharing their
782 help, time, and expertise as they each worked on their individual but related research projects.
783 We would also like to thank Mark Severson, Mark Jirsa, and Phil Larson for introducing L.
784 Brengman to the drill core repository, and for their helpful discussions over the last few years.
785 We are grateful for helpful feedback from Maxwell Lechte and an anonymous reviewer, which
786 has greatly improved this manuscript.

REFERENCES

Addison, W.D., Brumpton, G.R., Vallini, D.A., McNaughton, N.J., Davis, D.W., Kissin, S.A., Fralick, P.W., and Hammond, A.L. (2005) Discovery of distal ejecta from the 1850 Ma Sudbury impact event. Geology, 33, 193.

Akin, S.J., Pufahl, P.K., Hiatt, E.E., and Pirajno, F. (2013) Oxygenation of shallow marine environments and chemical sedimentation in Palaeoproterozoic peritidal settings: Frere Formation, Western Australia. (N. Sheldon, Ed.) Sedimentology, 60, 1559–1582.

Albut, G., Babechuk, M.G., Kleinhanns, I.C., Benger, M., Beukes, N.J., Steinhilber, B., Smith, A.J.B., Kruger, S.J., and Schoenberg, R. (2018) Modern rather than Mesoarchaean oxidative weathering responsible for the heavy stable Cr isotopic signatures of the 2.95 Ga old Ijzermijn iron formation (South Africa). Geochimica et Cosmochimica Acta, 228, 157–189.

Bekker, A., Slack, J.F., Planavsky, N., Krapez, B., Hofmann, A., Konhauser, K.O., and Rouxel, O.J. (2010) Iron Formation: The Sedimentary Product of a Complex Interplay among Mantle, Tectonic, Oceanic, and Biospheric Processes. Economic Geology, 105, 467–508.

Bekker, A., Planavsky, N.J., Krapež, B., Rasmussen, B., Hofmann, A., Slack, J.F., Rouxel, O.J., and Konhauser, K.O. (2014) Iron Formations: Their Origins and Implications for Ancient Seawater Chemistry. In Treatise on Geochemistry pp. 561–628. Elsevier.

Beukes, N.J. (1980). Lithofacies and stratigraphy of the Kuruman and Griquatown iron-formations, Northern Cape Province, South Africa. South African Journal of Geology, 83, 69-86.

808 Beukes, N.J., and Klein, C. (1990) Geochemistry and sedimentology of a facies transition —
809 from microbanded to granular iron-formation — in the early Proterozoic Transvaal
810 Supergroup, South Africa. Precambrian Research, 47, 99–139.

811 Brengman, L.A., Fedo, C.M., Whitehouse, M.J., Jabeen, I., and Banerjee, N.R. (2020) Textural,
812 geochemical, and isotopic data from silicified rocks and associated chemical sedimentary
813 rocks in the ~ 2.7 Ga Abitibi greenstone belt, Canada: Insight into the role of
814 silicification. Precambrian Research, 351, 105946.

815 Dimroth, E., and Chauvel, J.-J. (1973) Petrography of the Sokoman Iron Formation in Part of the
816 Central Labrador Trough, Quebec, Canada. GSA Bulletin, 84, 111–134.

817 Donovan, J.J., Allaz, J.M., von der Handt, A., Seward, G.G.E., Neill, O., Goemann, K.,
818 Chouinard, J., and Carpenter, P.K. (2021) Quantitative WDS compositional mapping
819 using the electron microprobe. American Mineralogist, 106, 1717–1735.

820 Dove, P., and Rimstidt, J. (1994) Silica: physical behavior, geochemistry and materials
821 applications. in “Silica-water interactions.” Reviews in Mineral, 29.

822 Duncanson, S.P., (2020) Identification of Primary and Diagenetic Mineralogy Preserved in
823 Silica-Cemented Horizons of the Biwabik Iron Formation, Minnesota, Using Petrography
824 and Electron Microprobe Analysis, 120 p. M.Sc. thesis, University of Minnesota, Duluth.

825 Eyster, A., Brengman, L.A., Nichols, C.I.O., Levitt, Z., Wilcots, J., and Bergmann, K.D. (2021)
826 A New Depositional Framework for Massive Iron Formations After the Great Oxidation
827 Event. Geochemistry, Geophysics, Geosystems, 22.

828 Fischer, W.W., and Knoll, A.H. (2009) An iron shuttle for deepwater silica in Late Archean and
829 early Paleoproterozoic iron formation. Geological Society of America Bulletin, 121, 222-
830 235.

831

832 Floran, R.J., and Papike, J.J. (1975) Petrology of the low-grade rocks of the Gunflint Iron-
833 Formation, Ontario-Minnesota. Geological Society of America Bulletin, 86, 1169–1190.

834 Floran, R.J., and Papike, J.J. (1978) Mineralogy and Petrology of the Gunflint Iron Formation,
835 Minnesota-Ontario: Correlation of Compositional and Assemblage Variations at Low to
836 Moderate Grade. Journal of Petrology, 19, 215–288.

837 Flügel, E., and Munnecke, A. (2010) Microfacies of carbonate rocks: analysis, interpretation and
838 application, 2nd ed., 984 p. Springer, Heidelberg ; New York.

839

840 Fralick, P., Davis, D.W., and Kissin, S.A. (2002) The age of the Gunflint Formation, Ontario,
841 Canada: single zircon U•Pb age determinations from reworked volcanic ash, 39, 11.

842 French, B.M. (1968) Bulletin No. 45. Progressive Contact Metamorphism of the Biwabik Iron-
843 formation, Mesabi Range, Minnesota.

844 French, B.M. (1973) Mineral Assemblages in Diagenetic and Low-Grade Metamorphic Iron-
845 Formation. Economic Geology, 68, 1063–1074.

Frost, C.D., von Blanckenburg, F., Schoenberg, R., Frost, B.R., and Swapp, S.M. (2007) Preservation of Fe isotope heterogeneities during diagenesis and metamorphism of banded iron formation. Contributions to Mineralogy and Petrology, 153, 211–235.

Gole, M.J. (1980) Mineralogy and petrology of very-low-metamorphic grade Archaean banded iron-formations, Weld Range, Western Australia. American Mineralogist, 65, 8–25.

Gumsley, A.P., Chamberlain, K.R., Bleeker, W., Söderlund, U., de Kock, M.O., Larsson, E.R., and Bekker, A. (2017) Timing and tempo of the Great Oxidation Event. Proceedings of the National Academy of Sciences, 114, 1811–1816.

Harder, H. (1978) Synthesis of Iron Layer Silicate Minerals under Natural Conditions. Clays and Clay Minerals, 26, 65–72.

Heaman, L.M., Easton, R.M. (2005) Proterozoic history of the Lake Nipigon area, Ontario: Constraints from U-Pb zircon and baddeleyite dating. 51st ILSG Annual Meeting, part 1, p. 24-25.

Heinrich, B., Urquhart, K., Arrott, A., Cochran, J., Myrtle, K., and Purcell, S. (1987) Ferromagnetic-resonance study of ultrathin bcc Fe (100) films grown epitaxially on fcc Ag (100) substrates. Physical review letters, 59, 1756.

Hemming, S., McLennan, S., Hanson, G., Krogstad, E., and Mezger, K. (1990) Pb isotope systematics in quartz. Eos, 71, 654–655.

Hinz, I.L., Nims, C., Theuer, S., Templeton, A.S., and Johnson, J.E. (2021) Ferric iron triggers greenalite formation in simulated Archean seawater. Geology, 49, 905-910.

866 Jiang, C.Z., and Tosca, N.J. (2019) Fe(II)-carbonate precipitation kinetics and the chemistry of
867 anoxic ferruginous seawater. Earth and Planetary Science Letters, 506, 231–242.

868 Jirsa, M.A., Miller, J.D., and Morey, G.B. (2008) Geology of the Biwabik Iron Formation and
869 Duluth Complex. Regulatory Toxicology and Pharmacology, 52, S5–S10.

870 Johnson, J.E., Muhling, J.R., Cosmidis, J., Rasmussen, B., and Templeton, A.S. (2018) Low-
871 Fe(III) Greenalite Was a Primary Mineral From Neoarchean Oceans. Geophysical
872 Research Letters, 45, 3182–3192.

873 Kipp, M.A., Stüeken, E.E., Bekker, A., and Buick, R. (2017) Selenium isotopes record extensive
874 marine suboxia during the Great Oxidation Event. Proceedings of the National Academy
875 of Sciences, 114, 875–880.

876 Klein, C. (2005) Some Precambrian banded iron-formations (BIFs) from around the world: Their
877 age, geologic setting, mineralogy, metamorphism, geochemistry, and origins. American
878 Mineralogist, 90, 1473–1499.

879 Konhauser, K.O., Planavsky, N.J., Hardisty, D.S., Robbins, L.J., Warchola, T.J., Haugaard, R.,
880 Lalonde, S.V., Partin, C.A., Oonk, P.B.H., Tsikos, H., and others (2017) Iron formations:
881 A global record of Neoarchaean to Palaeoproterozoic environmental history. Earth-
882 Science Reviews, 172, 140–177.

883 Krapež, B., Barley, M.E., and Pickard, A.L. (2003) Hydrothermal and resedimented origins of
884 the precursor sediments to banded iron formation: sedimentological evidence from the
885 Early Palaeoproterozoic Brockman Supersequence of Western Australia: Resedimented
886 origins of banded iron formation. Sedimentology, 50, 979–1011.

887 LaBerge, G.L. (1964) Development of magnetite in iron formations of the Lake Superior region.
888 Economic Geology, 59, 1313–1342.

889 Lafuente, B., Downs, R.T., Yang, H., and Stone, N. (2015) 1. The power of databases: The
890 RRUFF project. In Highlights in mineralogical crystallography pp. 1–30. De Gruyter (O).

891 Lantink, M.L., Oonk, P.B., Floor, G.H., Tsikos, H., and Mason, P.R. (2018) Fe isotopes of a 2.4
892 Ga hematite-rich IF constrain marine redox conditions around the GOE. Precambrian
893 Research, 305, 218–235.

894 Leith, C.K. (1903) The Mesabi iron-bearing district of Minnesota Vol. 43. US Government
895 Printing Office.

896 Lucente, M.E., and Morey, G.B. (1983) Stratigraphy and sedimentology of the Lower
897 Proterozoic Virginia Formation, northern Minnesota: Minnesota Geological Survey Report of
898 Investigations 28, 28 p.

899 Losh, S., and Rague, R. (2018) Hydrothermal oxidation in the Biwabik Iron Formation, MN,
900 USA. Mineralium Deposita, 53, 1143–1166.

901 Lowenstein, T.K., Kendall, B., and Anbar, A. (2013) The geologic history of seawater. In The
902 Oceans and Marine Geochemistry pp. 569–622. Elsevier Inc.

903 Lyons, T.W., Reinhard, C.T., and Planavsky, N.J. (2014) The rise of oxygen in Earth's early
904 ocean and atmosphere. Nature, 506, 307–315.

905 Lyons, T.W., Diamond, C.W., Planavsky, N.J., Reinhard, C.T., and Li, C. (2021) Oxygenation,
906 Life, and the Planetary System during Earth's Middle History: An Overview.
907 Astrobiology, 21, 906–923.

908 Maliva, R.G., Knoll, A.H., and Simonson, B.M. (2005) Secular change in the Precambrian silica
909 cycle: Insights from chert petrology. Geological Society of America Bulletin, 117, 835.

910 McSwiggen, P.L., and Morey, G.B. (2008) Overview of the mineralogy of the Biwabik Iron
911 Formation, Mesabi Iron Range, northern Minnesota. Regulatory Toxicology and
912 Pharmacology, 52, S11–S25.

913 Milesi, V., Guyot, F., Brunet, F., Richard, L., Recham, N., Benedetti, M., Dairou, J., and
914 Prinzhofer, A. (2015) Formation of CO2, H2 and condensed carbon from siderite
915 dissolution in the 200–300°C range and at 50MPa. Geochimica et Cosmochimica Acta,
916 154, 201–211.

917 Morey, G.B. (1992) Chemical composition of the eastern Biwabik Iron-Formation (early
918 Proterozoic), Mesabi Range, Minnesota. Economic Geology, 87, 1649–1658.

919 Muhling, J.R., and Rasmussen, B. (2020) Widespread deposition of greenalite to form Banded
920 Iron Formations before the Great Oxidation Event. Precambrian Research, 339, 105619.

921 Ojakangas, R.W. (1983) Tidal deposits in the early Proterozoic basin of the Lake Superior
922 region—The Palms and the Pokegama Formations: Evidence for subtidal-shelf deposition
923 of Superior-type banded iron-formation. Geological Society of America Memoir, 160,
924 49–66.

925 Ojakangas, R.W., Morey, G.B., and Southwick, D.L. (2001) Paleoproterozoic basin development
926 and sedimentation in the Lake Superior region, North America. Sedimentary Geology,
927 141–142, 319–341.

928 Ojakangas, R.W., Severson, M.J., and Jongewaard, P.K. (2011) Geology and sedimentology of
929 the Paleoproterozoic Animikie Group: The Pokegama Formation, the Biwabik Iron
930 Formation, and Virginia Formation of the eastern Mesabi Iron Range and Thomson
931 Formation near Duluth, northeastern Minnesota. In Archean to Anthropocene: Field
932 Guides to the Geology of the Mid-Continent of North America pp. 101–120. Geological
933 Society of America.

934 Pecoits, E., Gingras, M.K., Barley, M.E., Kappler, A., Posth, N.R., and Konhauser, K.O. (2009)
935 Petrography and geochemistry of the Dales Gorge banded iron formation: Paragenetic
936 sequence, source and implications for palaeo-ocean chemistry. Precambrian Research,
937 172, 163–187.

938 Planavsky, N., Rouxel, O., Bekker, A., Shapiro, R., Fralick, P., and Knudsen, A. (2009) Iron-
939 oxidizing microbial ecosystems thrived in late Paleoproterozoic redox-stratified oceans.
940 Earth and Planetary Science Letters, 286, 230–242.

941 Planavsky, N.J., Bekker, A., Hofmann, A., Owens, J.D., and Lyons, T.W. (2012) Sulfur record
942 of rising and falling marine oxygen and sulfate levels during the Lomagundi event.
943 Proceedings of the National Academy of Sciences, 109, 18300–18305.

Posth, N.R., Köhler, I., D. Swanner, E., Schröder, C., Wellmann, E., Binder, B., Konhauser, K.O., Neumann, U., Berthold, C., Nowak, M., and others (2013) Simulating Precambrian banded iron formation diagenesis. Chemical Geology, 362, 66–73.

Pouchou, J.-L., and Pichoir, F. (1991) Quantitative analysis of homogeneous or stratified microvolumes applying the model "PAP." In Electron probe quantitation pp. 31–75. Springer.

Poulton, S.W., Bekker, A., Cumming, V.M., Zerkle, A.L., Canfield, D.E., and Johnston, D.T. (2021) A 200-million-year delay in permanent atmospheric oxygenation. Nature, 592, 232–236.

Pufahl, P.K., Anderson, S.L., and Hiatt, E.E. (2014) Dynamic sedimentation of Paleoproterozoic continental margin iron formation, Labrador Trough, Canada: Paleoenvironments and sequence stratigraphy. Sedimentary Geology, 309, 48–65.

Rasmussen, B., and Muhling, J.R. (2018) Making magnetite late again: Evidence for widespread magnetite growth by thermal decomposition of siderite in Hamersley banded iron formations. Precambrian Research, 306, 64–93.

——— (2020) Hematite replacement and oxidative overprinting recorded in the 1.88 Ga Gunflint iron formation, Ontario, Canada. Geology, 48, 688-692.

Rasmussen, B., Meier, D.B., Krapež, B., and Muhling, J.R. (2013) Iron silicate microgranules as precursor sediments to 2.5-billion-year-old banded iron formations. Geology, 41, 435–438.

964 Rasmussen, B., Krapez, B., and Meier, D.B. (2014) Replacement origin for hematite in 2.5 Ga
965 banded iron formation: Evidence for postdepositional oxidation of iron-bearing minerals.
966 Geological Society of America Bulletin, 126, 438–446.

967 Rasmussen, B., Krapež, B., and Muhling, J.R. (2015) Seafloor silicification and hardground
968 development during deposition of 2.5 Ga banded iron formations. Geology, 43, 235–238.

969 Rasmussen, B., Muhling, J.R., Suvorova, A., and Krapež, B. (2016) Dust to dust: Evidence for
970 the formation of "primary" hematite dust in banded iron formations via oxidation of iron
971 silicate nanoparticles. Precambrian Research, 284, 49–63.

972 ——— (2017) Greenalite precipitation linked to the deposition of banded iron formations
973 downslope from a late Archean carbonate platform. Precambrian Research, 290, 49–62.

974 Rasmussen, B., Muhling, J.R., and Fischer, W.W. (2019) Evidence from laminated chert in
975 banded iron formations for deposition by gravitational settling of iron-silicate muds.
976 Geology, 47, 167–170.

977 Rasmussen, B., Muhling, J.R., and Krapež, B. (2021) Greenalite and its role in the genesis of
978 early Precambrian iron formations – A review. Earth-Science Reviews, 103613.

979 Robbins, L.J., Funk, S.P., Flynn, S.L., Warchola, T.J., Li, Z., Lalonde, S.V., Rostron, B.J.,
980 Smith, A.J.B., Beukes, N.J., de Kock, M.O., and others (2019) Hydrogeological
981 constraints on the formation of Palaeoproterozoic banded iron formations. Nature
982 Geoscience, 12, 558–563.

983 Schneider, C.A., Rasband, W.S., and Eliceiri, K.W. (2012) NIH Image to ImageJ: 25 years of
984 image analysis. Nature Methods, 9, 671–675.

985 Schulz, K.J., and Cannon, W.F. (2007) The Penokean orogeny in the Lake Superior region.
986 Precambrian Research, 157, 4–25.

987 Severson, M.J., Heine, J.J., and Patelke, M.M. (2009) Geologic and Stratigraphic Controls of the
988 Biwabik Iron Formation and the Aggregate Potential of the Mesabi Iron Range, Minnesota.
989 University of Minnesota Duluth, Natural Resources Research Institute, Technical Report
990 NRRI/TR-2009/09, 173 p. + 37 plates.

991 Sheppard, S., Krapež, B., Zi, J.-W., Rasmussen, B., and Fletcher, I.R. (2017) Young ores in old
992 rocks: Proterozoic iron mineralisation in Mesoarchean banded iron formation, northern
993 Pilbara Craton, Australia. Ore Geology Reviews, 89, 40–69.

994 Siever, R. (1992) The silica cycle in the Precambrian. Geochimica et Cosmochimica Acta, 56,
995 3265–3272.

996 Simonson, B.M., (1987) Early Silica Cementation and Subsequent Diagenesis in Arenites from
997 Four Early Proterozoic Iron Formations of North America. SEPM Journal of Sedimentary
998 Research, 57, 494–511.

999 Southwick, D., and Day, W. (1983) Geology and petrology of Proterozoic mafic dikes, north-
1000 central Minnesota and western Ontario. Canadian Journal of Earth Sciences, 20, 622–
1001 638.

1002 Stefurak, E.J.T., Lowe, D.R., Zentner, D., and Fischer, W.W. (2014) Primary silica granules—A
1003 new mode of Paleoarchean sedimentation. Geology, 42, 283–286.

1004 ——— (2015) Sedimentology and geochemistry of Archean silica granules. Geological Society
1005 of America Bulletin, 127, 1090–1107.

1006 Sturesson, U., Heikoop, J.M., and Risk, M.J. (2000) Modern and Palaeozoic iron ooids—a
1007 similar volcanic origin. Sedimentary Geology, 136, 137–146.

1008 Todd, S.E., Pufahl, P.K., Murphy, J.B., and Taylor, K.G. (2019) Sedimentology and
1009 oceanography of Early Ordovician ironstone, Bell Island, Newfoundland: Ferruginous
1010 seawater and upwelling in the Rheic Ocean. Sedimentary Geology, 379, 1–15.

1011 Tosca, N.J., Guggenheim, S., and Pufahl, P.K. (2016) An authigenic origin for Precambrian
1012 greenalite: Implications for iron formation and the chemistry of ancient seawater.
1013 Geological Society of America Bulletin, 128, 511–530.

1014 Tosca, N.J., Jiang, C.Z., Rasmussen, B., and Muhling, J. (2019) Products of the iron cycle on the
1015 early Earth. Free Radical Biology and Medicine, 140, 138-153.

1016 van de Velde, S.J., Reinhard, C.T., Ridgwell, A., and Meysman, F.J. (2020) Bistability in the
1017 redox chemistry of sediments and oceans. Proceedings of the National Academy of
1018 Sciences, 117, 33043–33050.

1019 Wacey, D., Eiloart, K., and Saunders, M. (2021) Pathways of microfossil mineralisation by
1020 hematite in the 1878 Ma Gunflint Formation. Chemical Geology, 581, 120419.

Wilson, J.P., Fischer, W.W., Johnston, D.T., Knoll, A.H., Grotzinger, J.P., Walter, M.R., McNaughton, N.J., Simon, M., Abelson, J., Schrag, D.P., and others (2010) Geobiology of the late Paleoproterozoic Duck Creek Formation, Western Australia. Precambrian Research, 179, 135–149.

Wintsch, R.P., and Kvale, C.M. (1994) Differential Mobility of Elements in Burial Diagenesis of Siliciclastic Rocks. SEPM Journal of Sedimentary Research, 64A, 349–361.

Wolff, J. (1917) Recent geologic developments on the Mesabi iron range, Minnesota. American Institute of Mining and Metallurgical Engineers, Transactions, 56, p. 229-257.

Figure Captions

Figure 1. Mineralogy studies identifying primary Fe-silicates among silica-cemented horizons in iron formations through Earth history. (A) Si-cement study references come from Rasmussen and Muhling (2021), and are 1= Rasmussen et al. (2014b); 2= Muhling and Rasmussen (2020) 3= Sheppard et al. (2017); 4= Rasmussen et al. (2015); 5= Rasmussen et al. (2017); 6= Beukes (1980), 7= Tosca et al. (2019); 8= Lantink et al. (2018). (B) Atmospheric oxygen concentrations from Lyons et al. 2021. (C) Simplified ocean chemistry adapted from Lowenstein et al. (2013) and van de Velde et al. (2020). (D) Distribution of marine iron formation deposits in billion metric tons (Gt), modified from Bekker et al. (2014), based on data from Bekker et al. (2010.) Asterix and lighter color boxes represent units with poor age constraints.

Figure 2. Simplified Archean-Proterozoic bedrock geology of Northeastern Minnesota including Mesabi and Gunflint Iron Ranges. The star denotes location of drill cores sampled for this study. Modified from Jirsa et al. (2007) and Poulton et al. (2010). (A) Regional schematic showing the geographic location of the Animikie Basin and associated Mesabi iron range. (B) Simplified geologic map showing the relationship between rocks of the Animikie Basin and surrounding rocks. (C) Graphic log of drill cores LWD-99-01 and LWD-99-02 from the star locations in B. Petrography samples denoted by circle symbols, stars represent samples with EPMA data. Depth is noted as feet and as meters below surface. Drill core logs based on observational data and Severson et al. (2009.)

Figure 3. Example of a silica-cemented horizons in the Biwabik Iron Formation. (A) Drill core showing a chert nodule and the surrounding fine-grained, banded horizons. Note the sediment

draping around a silica nodule. The sample comes from the Lower Cherty, a unit defined by granular textures overall. (B) Photomicrograph composite map of the same chert nodule as (A). The chert nodule preserves granular textures and quartz cement. Within silica-cemented nodules, a higher density of iron phases between granules are often observed proximal to the banded horizons (nodule margin) relative to the nodule center. (C) Drill core photo showing chert nodule and surrounding thin banded horizons. (D) Close up photomicrograph composite map of the area outlined by the square in (C) showing preservation of granular textures in silica-cemented nodules. The sample comes from the Lower Cherty, a unit that predominantly contains banded textures.

Figure 4. Electron microprobe point data from chamosite (A), stilpnomelane (B), minnesotaite (C) and greenalite (D). Samples are separated based on mineralogy and textural relationships (described in the text), and "n" refers to the number of point analyses per sample.

Figure 5. Representative examples of chamosite textures preserved in silica-cemented horizons and banded horizons. (A) Si-cemented horizon (sample MIR-19-12) showing zonation (zones 1-3). Granules in zones 1 and 3 are predominantly chamosite, while granules in zone 2 have less chamosite, and are primarily composed of chert. (B) Photomicrograph showing chamosite (chm) occurring as granules in Si-cemented (qtz) and banded horizons (sample MIR-19-15). Granules near the banded horizon often contain stilpnomelane (stp) as well (C) Plane-polarized light photomicrograph showing chamosite occurring within banded horizons (sample MIR-19-15). (D) Back-scattered electron image showing chamosite (chm) and a carbonate crystal (cb) cross-cut by stilpnomelane (stp).

Figure 6. Representative examples of minnesotaite textures preserved in Si-cemented horizons. (A) Cross-polarized light photomicrograph composite map of sample MIR-L-07 showing granular vs. banded textures. (B) Close-up photomicrograph of square in (A) showing greenalite granules with minnesotaite (mns) as cement and intergranular phases (sample MIR-L-07). (C) Composite photomicrograph (cross-polarized light) of sample MIR-19-05 showing minnesotaite granules. (D) Close up of square in (C) of minnesotaite granule (mns 1) and cement (mns 2). Note cross-cutting magnetite (mt). (E) Plane-polarized light photomicrograph composite map of Si-cemented horizons (chert nodule) in sample MIR-19-3.5. (F) Back-scattered electron image of minnesotaite (mns) granule preserved inside the Si-cemented horizon in (D). (G) Back-scattered electron image of stilpnomelane (stp) granule preserved at the edge of the chert nodule (D), near the banded layer. Note the cross-cutting relationship between magnetite (mt) and stilpnomelane (stp).

Figure 7. Representative examples of greenalite textures and greenalite-minnesotaite textural relationships preserved in Si-cemented horizons and Raman spectra of greenalite and minnesotaite. (A) Plane-polarized light composite photomicrograph map of sample MIR-U-10. (B) Close-up, plane-polarized light photomicrograph map of square area in (A) showing greenalite granules. (C) Back-scattered electron image of square area in (B) showing greenalite granules. (D and E) Close-up back-scattered electron images of square areas in (C) showing greenalite granule (gre) and minnesotaite cement (mns in D) as well as minor compositional

variation (x) internal to greenalite (gre) granules (E)). (F) Back-scatter electron image of granules composed of greenalite aggregates (gre) and minnesotaite (mns) cement (sample MIR-L-07)). (G) Close-up back-scattered electron image of square area in (F) showing greenalite granule (gre) and minnesotaite cement (mns) growing into non-compaction fracture (now quartz-cemented, arrows). (H) Raman spectra for areas 1 (mns) and 2 (gre) in (D) and 3 (mns) and 4 (gre) in (G).

Figure 8. Additional examples of greenalite textures and greenalite-minnesotaite textural relationships preserved in Si-cemented horizons with Raman spectra across a granule-cement transect. (A) Cross-polarized light composite photomicrograph map of sample MIR-17-13 showing mixed greenalite-minnesotaite granules. (B) Back-scattered electron image of square area in (A) containing granules composed of greenalite and acicular minnesotaite among dark-gray quartz cement. (C) Back-scattered electron image of granule with minnesotaite (mns) cement nucleating off granule boundaries (sample MIR-17-13). (D) Close-up photomicrograph of rectangle in (B). (E) Raman spectra transect across granule-cement contact (numbered line in D)). (F) Mineral map of Raman spectra from area (F) showing both primarily greenalite and mixed greenalite-minnesotaite granules with minnesotaite and quartz cement. (G) Cherty granule with dusty appearance due to presence of disseminated sub μm greenalite crystals (sample MIR-17-18). (H) Back-scattered electron image of square area in (G) showing fine-grained, disseminated Fe-oxides and greenalite next to a quartz filled non-compaction fracture (qtz ncf). (I) Composite SEM K-alpha element map acquired with EDS showing Fe and Si distributions in the same field of view as (H).

Figure 9. Representative examples of cross-cutting relationships between carbonates, Fe-oxides, and silicate phases. (A) Cross-polarized photomicrograph showing large, euhedral carbonate, and > 5 μm hematite laths cross-cutting chert granules. (B) Back-scattered electron image showing an example of minnesotaite (mns) cross-cutting carbonates (carb.) with variable Ca-Fe-Mg composition (white dashed lines and black dashed lines). (C) Plane-polarized light photomicrograph showing a chert intraclast with carbonate crystals (carb.) inside the intraclast. (D) Cross-polarized light photomicrograph of a different chert intraclast with carbonate crystals (carb.; larger than those in C). (E) Altered granule showing magnetite (mt) cross-cutting minnesotaite (mns) and carbonate (carb.), forming rims around replaced granules. (F) Back-scattered electron image showing >5 μm hematite laths and fine-grained hematite (hm, arrows), and large, euhedral magnetite (mt) cross-cutting fine-grained iron silicate phases (chamosite, chm). Stilpnomelane (stp) is also shown cross-cutting chamosite (chm) in the same image). (G) Close-up image of phase relationships demonstrated in (F). (H) Back-scattered electron image of a quartz grain (qtz) coated with multiple layers of fine-grained hematite (hm).

Figure 10. Proposed diagenetic model for Fe-silicate mineral assemblages in the Biwabik Iron Formation. (A) Initial sediment deposition includes mixed $Fe^{2+,3+}$-Si-O-OH gel, terrigenous-sourced sediment, and the possibility for addition of Si through diffusion of silicic acid (H_4SiO_4) into the sediment. (B) Post-deposition, but still during early diagenesis, several different mineral reaction sets may take place (B_1-B_3) depending on the nature and degree of silica-addition through silicification, and original presence of terrigenous sediment. References for reactions outlined in sequences B_1- B_3 are as follow: (1,2) Posth et al. 2013; (3) French 1973; (4) Tosca et al. 2019; (5) Milesi et al. 2015; Rasmussen et al. 2018; (6) Dove and Rimstidt 1994; (7) Klein

2005; this study; (8) Gole 1980; (9) Tosca et al. 2016; (10) Klein 2005; (11) Floran and Papike 1978. (C) Reactions from (B) lead to the present mineralogy observed in the sample sets. Minerals and sediments are not to scale.

Supplementary Figure S1 caption.

Figure S1. Summary of locations and mineralogy of individual EPMA point analyses in thin section samples MIR-17-21, MIR-17-19, MIR-U-10 and MIR-17-16. (A-D) TL images of samples. (E-H): BSE images of point analysis areas. The chert intraclast in H is traced with a dashed outline. (I) FeO-MgO-Cao ternary diagram. Gray-colored triangles are from two carbonate-bearing rock types in the Stambaugh Formation (Planavsky et al. 2018).

1154 Table 1. Samples for electron probe microanalysis.

Unit	Sample	Core ft.	Mineral phase(s) targeted for EPMA point analysis	General description of phase for EPMA point analysis
Upper Slaty	MIR-17-18	587'	chamosite, siderite, ankerite-dolomite	(1) Chamosite granules in banded horizon (2) carbonate rhombs in chert intraclast (3) carbonate phases among veins
	MIR-17-16	617'	stilpnomelane	Stilpnomelane crystals in chert intraclast
	MIR-17-15	622'	chamosite	Chamosite granules among banded horizons
Upper Cherty	MIR-19-15 (99-2)	872'	chamosite	Chamosite granules among silica-cemented and banded horizons
	MIR-17-13	647'	minnesotaite	(1) Granules among silica-cement (2) Minnesotaite cement
Lower Slaty	MIR-19-05	889'	minnesotaite	(1) Granules among silica-cement (2) Minnesotaite cement
	U-07	893'	siderite	Carbonate rhombs encrusted in magnetite
	U-08	908'	stilpnomelane, minnesotaite	(1) Stilpnomelane granules among banded horizon (2) Minnesotaite granules among silica-cement
Lower Cherty	U-10	1060'	greenalite, minnesotaite, siderite	(1) Greenalite granules (2) Micritic siderite (3) Minnesotaite cement
	L-07	1221'	greenalite, minnesotaite	(1) Greenalite granules (2) Minnesotaite cement
	MIR-19-12 (99-2)	1394'	chamosite	Granules inside and outside silica-cemented nodule
	MIR-19-3.5	1247'	stilpnomelane, minnesotaite	(1) Minnesotaite granules inside silica-cemented nodule (2) Stilpnomelane granules among edge of nodule

1155
1156
1157
1158

1159 Table 2. The typical habits and distribution of common minerals among silica-cemented and
1160 banded horizons.

Mineral	Crystal habit	Distribution among silica-cemented and banded horizons
Fe-silicates		
Greenalite	sub-µm crystals, appearing within granules as either disseminated crystals floating among chert or as aggregates of greenalite crystals	Internally within granules among silica- cemented horizons
Chamosite	aggregates of sub-µm crystals within granules	Internally within granules among silica-cemented and banded horizons
Minnesotaite	~3-50 µm euhedral-subhedral acicular sheaves within granules and among pore space	Within granules and as interstitial cement in silica-cemented horizons
Stilpnomelane	~3-100 µm acicular crystals within granules and among pore space	Within granules and as interstitial cement in silica-cemented and banded horizons
Carbonates		
Calcite	~5-15 µm micritic cement	Non-granular iron formation carbonate horizon
Ankerite-dolomite	~5-15 µm micritic cement, ~0.1 - 5 mm euhedral-subhedral rhombohedral	Micritic cement among banded horizons, rhombohedral among silica-cemented and banded horizons
Siderite	~5-15 µm micritic cement, ~100µm - 5 mm euhedral-subhedral rhombohedral	Micritic cement among banded horizons, rhombohedral among silica-cemented and banded horizons
Fe-oxides		
Hematite	sub-µm crystals, or as ≥5 µm subhedral plates	Both habits found among silica-cemented and banded horizons
Magnetite	~10-20 µm euhedral cubes	Found among silica-cemented and banded horizons

1161

1162 Table 3. Electron Microprobe analyses of average Fe-silicate composition and formulae ions.

	Chamosite						Minnesotaite				Stilpnomelane			Greenalite	
Sample (MIR)	**17-15**	**17-18**	**19-12**	**19-15**	**L-07**	**U-10**	**17-13**	**19-05**	**19-3.5**	**U-08**	**19-3.5**	**U-08**	**17-16**	**L-07**	**U-10**
# of points (n)	n = 20	n = 11	n = 20	n = 17	n = 14	n = 2	n = 22	n = 25	n = 13	n = 5	n = 6	n = 8	n = 3	n = 10	n = 10
Na_2O	0.04	0.03	0.03	0.1	0.03	0.04	0.01	0	0.06	0.02	0.37	0.18	0.43	0.06	0.05
MgO	4.02	5.92	7.37	13.55	6.73	4.24	1.63	7.33	19.5	19.75	10.84	12.77	3.01	5.86	3.11
SiO_2	24.83	24.36	25.02	29.72	53.37	51.94	49.09	52.73	56.21	56.78	42.84	48.59	46.93	34.35	33.35
Al_2O_3	13.93	16.74	15.9	11.7	0.64	0.23	0.23	0.11	0.56	0.47	3.45	4.32	4.54	2.32	0.95
K_2O	0.02	0.02	0	0.13	0.35	0.16	0.09	0.06	0.11	0.05	1.82	1.09	1.75	0.03	0.01
CaO	0.15	0.05	0.14	0.17	0.01	-0.02	0.04	0	0.11	0.04	0.04	0.05	0.04	0.18	0.18
FeO	43.78	40.52	38.79	30.54	32.55	36.88	42.21	32.88	17.2	16.61	25.85	24.84	33.58	44.61	51.18
MnO	0.08	0.03	0.16	0.2	0.09	0.14	0.04	0.05	0.03	0.02	0.17	0.1	0.15	0.16	0.27
O	0	9.48	10.24	10.71	5.33	7.34	5.63	5.23	4.7	4.44	15.76	7.92	8.73	7.97	8.67
Oxide total	99.80	97.13	97.66	96.82	99.1	100.93	98.99	98.4	98.49	98.17	101.14	99.88	99.15	95.55	97.77
Average formula															
Si	2.96	2.81	2.86	3.32	4.08	4.06	3.94	4.04	3.92	3.95	3.41	3.57	3.82	4.14	4.06
Fe	4.36	3.9	3.72	2.86	2.08	2.41	2.84	2.11	1	0.97	1.72	1.53	2.28	4.49	5.22
Mg	0.71	1.02	1.26	2.26	0.77	0.49	0.19	0.84	2.03	2.05	1.29	1.4	0.21	1.04	0.56
Mn	0.01	0	0.02	0.02	0.01	0.01	0	0	0	0	0.01	0.01	0.01	0.02	0.03
Al	1.96	2.27	2.15	1.54	0.06	0.02	0.02	0.01	0.05	0.04	0.32	0.37	0.43	0.32	0.14
K	-	-	-	-	-	-	-	-	-	-	0.19	0.1	0.18	-	-
Na	-	-	-	-	-	-	-	-	-	-	0.06	0.03	0.07	-	-
O	10	10	10	10	10	10	10	10	10	10	12	12	12	10	10
(OH)	8	8	8	8	2	2	2	2	2	2	1	1	1	8	8

1163

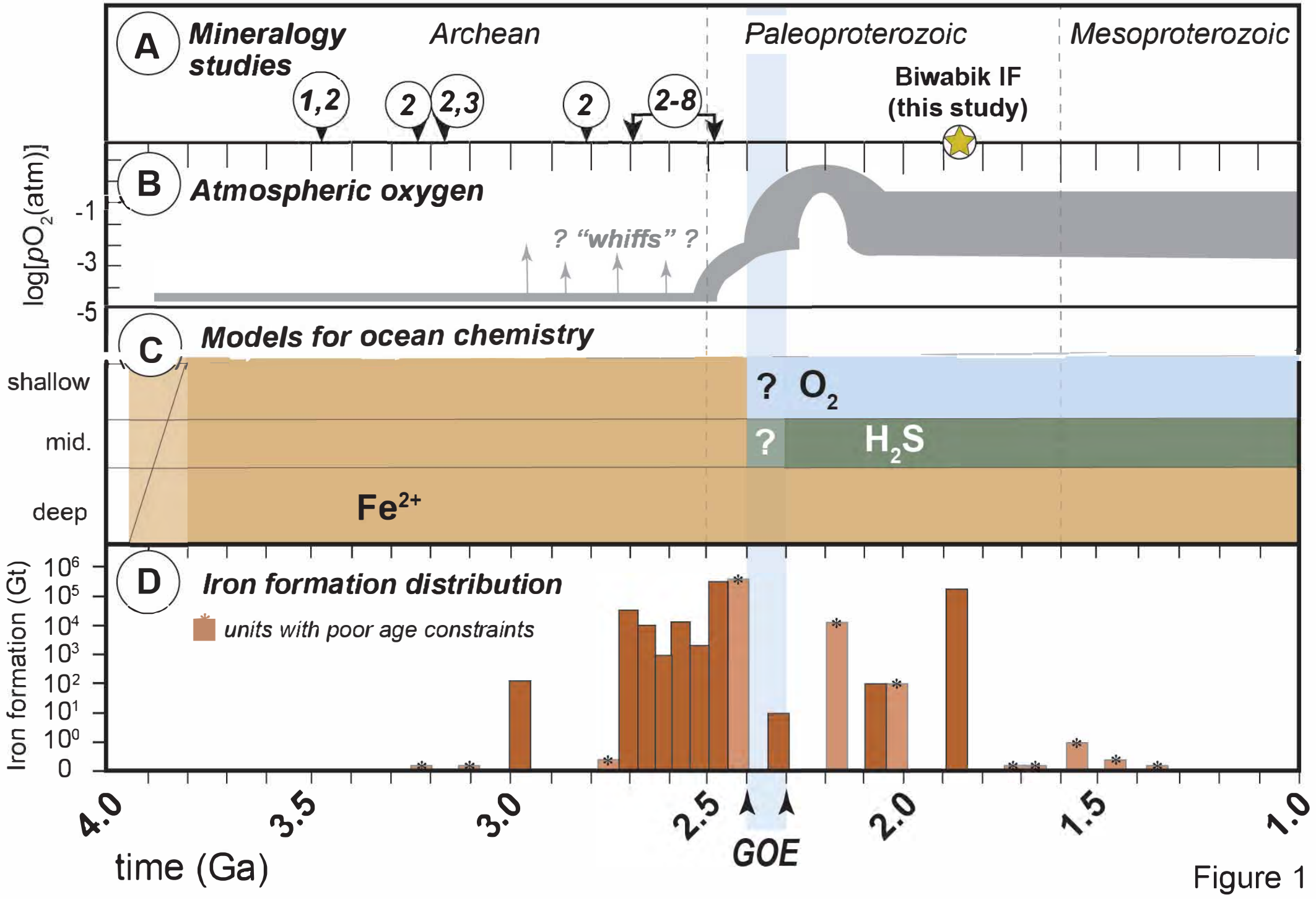
A
Mineralogy studies
Archean
Paleoproterozoic
Mesoproterozoic
1,2
2
2,3
2
2-8
Biwabik IF
(this study)
B
Atmospheric oxygen
log[pO2(atm)]
-1
-3
-5
? "whiffs" ?
C
Models for ocean chemistry
shallow
mid.
deep
? O2
? H2S
Fe2+
D
Iron formation distribution
units with poor age constraints
Iron formation (Gt)
10^6
10^5
10^4
10^3
10^2
10^1
10^0
0
4.0
3.5
3.0
2.5
2.0
1.5
1.0
GOE
time (Ga)

Figure 1

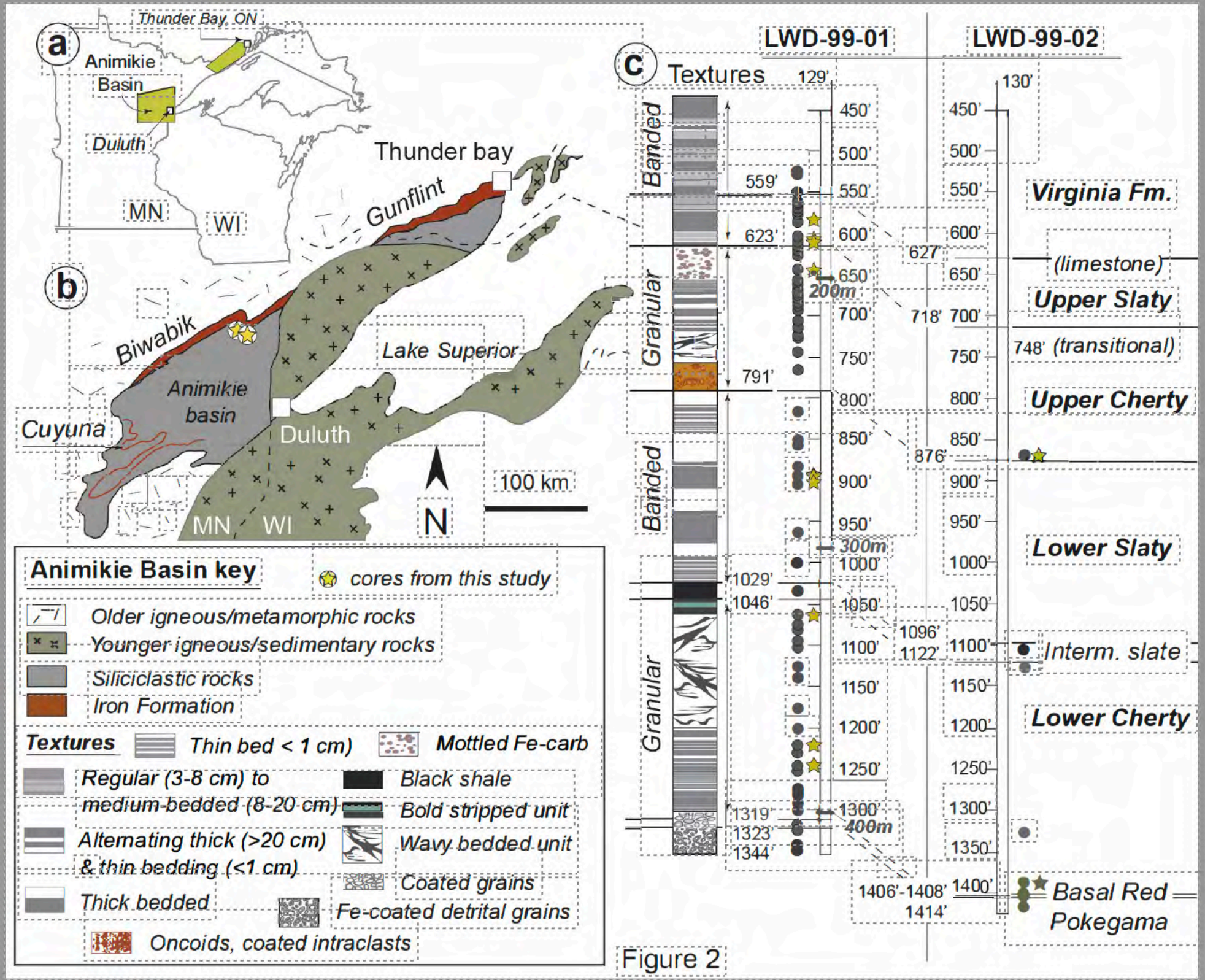
a
Thunder Bay, ON
Animikie Basin
Duluth
MN
WI
Thunder bay
Gunflint
b
Biwabik
Animikie basin
Cuyuna
Duluth
Lake Superior
MN
WI
N
100 km
Animikie Basin key
cores from this study
Older igneous/metamorphic rocks
Younger igneous/sedimentary rocks
Siliciclastic rocks
Iron Formation
Textures
Thin bed < 1 cm)
Mottled Fe-carb
Regular (3-8 cm) to medium-bedded (8-20 cm)
Black shale
Bold stripped unit
Alternating thick (>20 cm) & thin bedding (<1 cm)
Wavy bedded unit
Coated grains
Thick bedded
Fe-coated detrital grains
Oncoids, coated intraclasts
c
Textures
LWD-99-01
LWD-99-02
Banded
Granular
Banded
Granular
129'
559'
623'
791'
1029'
1046'
1319'
1323'
1344'
130'
627'
718'
748'
876'
1096'
1122'
1406'-1408'
1414'
200m
300m
400m
Virginia Fm.
(limestone)
Upper Slaty
(transitional)
Upper Cherty
Lower Slaty
Interm. slate
Lower Cherty
Basal Red
Pokegama

Figure 2

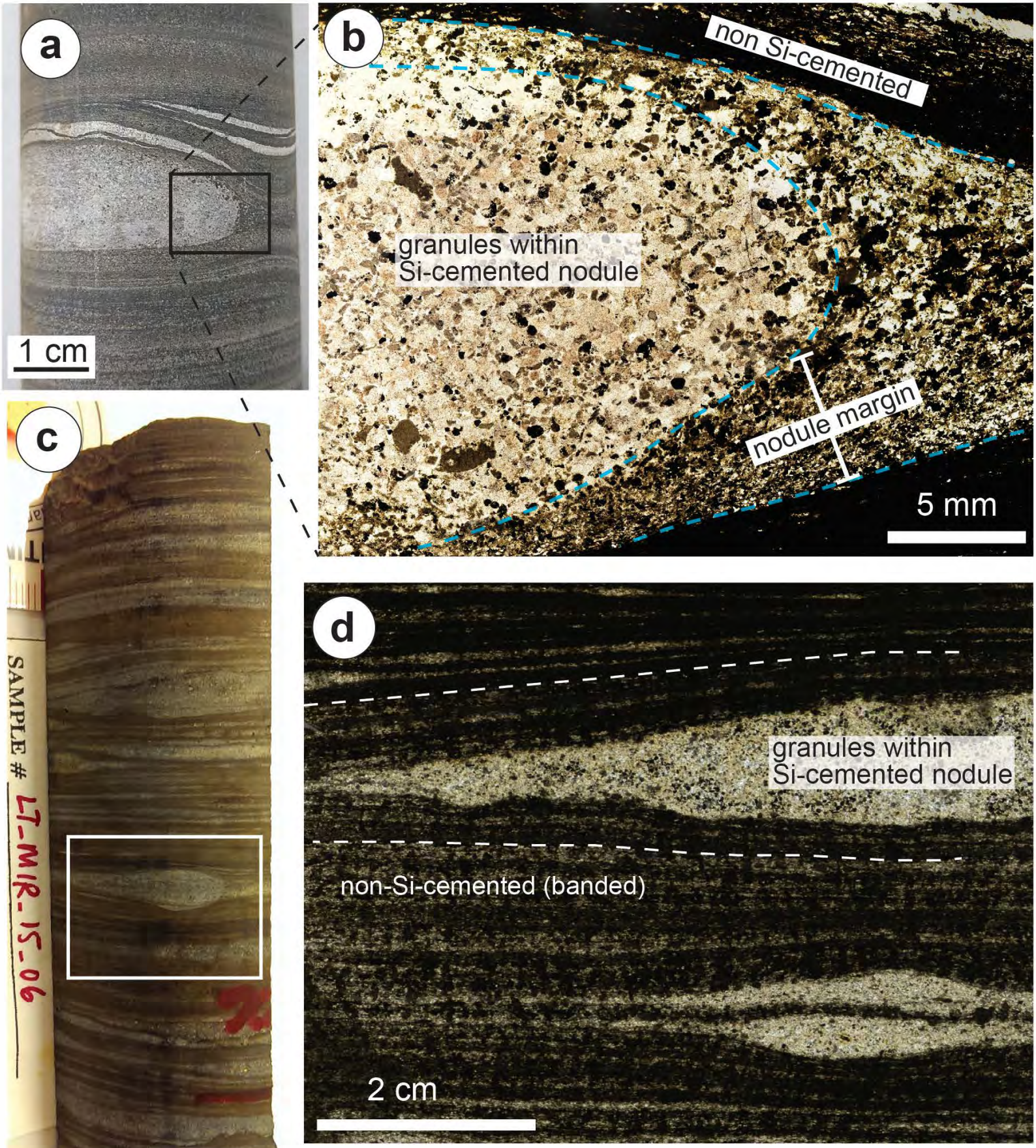
a
1 cm
b
non Si-cemented
granules within
Si-cemented nodule
nodule margin
5 mm
c
SAMPLE # LT-MIR-IS-06
1 cm
d
granules within
Si-cemented nodule
non-Si-cemented (banded)
2 cm

Figure 3

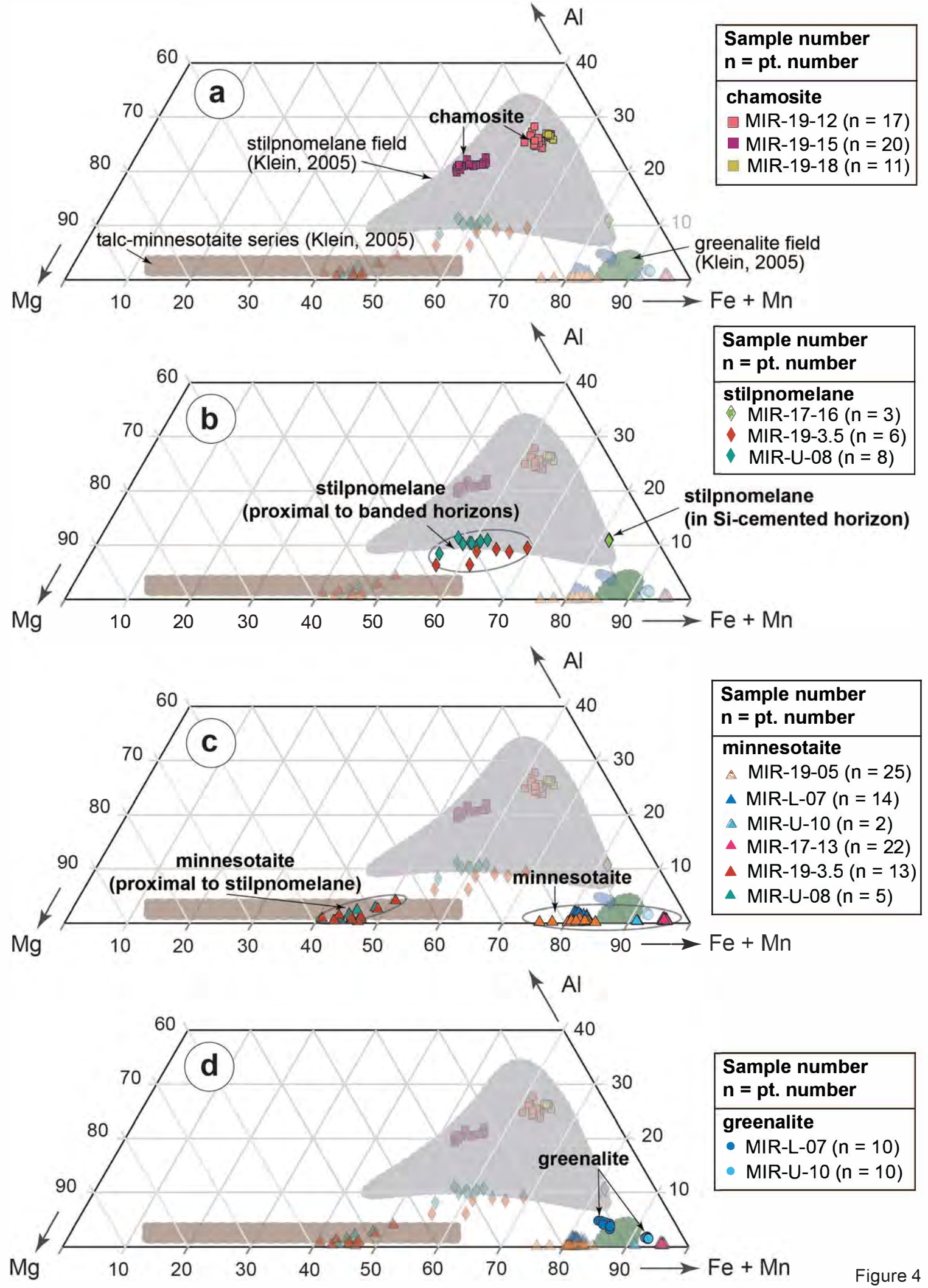
a
Al
Mg
Fe + Mn
chamosite
stilpnomelane field
(Klein, 2005)
talc-minnesotaite series (Klein, 2005)
greenalite field
(Klein, 2005)
Sample number
n = pt. number
chamosite
MIR-19-12 (n = 17)
MIR-19-15 (n = 20)
MIR-19-18 (n = 11)
b
stilpnomelane
(proximal to banded horizons)
stilpnomelane
(in Si-cemented horizon)
Sample number
n = pt. number
stilpnomelane
MIR-17-16 (n = 3)
MIR-19-3.5 (n = 6)
MIR-U-08 (n = 8)
c
minnesotaite
(proximal to stilpnomelane)
minnesotaite
Sample number
n = pt. number
minnesotaite
MIR-19-05 (n = 25)
MIR-L-07 (n = 14)
MIR-U-10 (n = 2)
MIR-17-13 (n = 22)
MIR-19-3.5 (n = 13)
MIR-U-08 (n = 5)
d
greenalite
Sample number
n = pt. number
greenalite
MIR-L-07 (n = 10)
MIR-U-10 (n = 10)

Figure 4

Figure 5

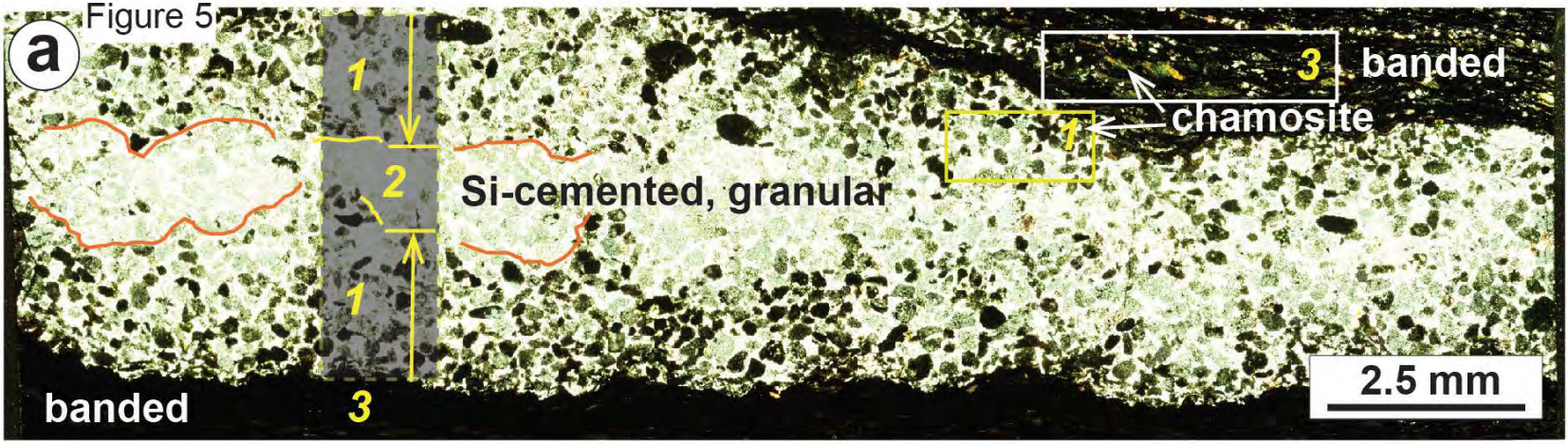
a
1
2
1
3
banded
Si-cemented, granular
3
banded
chamosite
1
2.5 mm

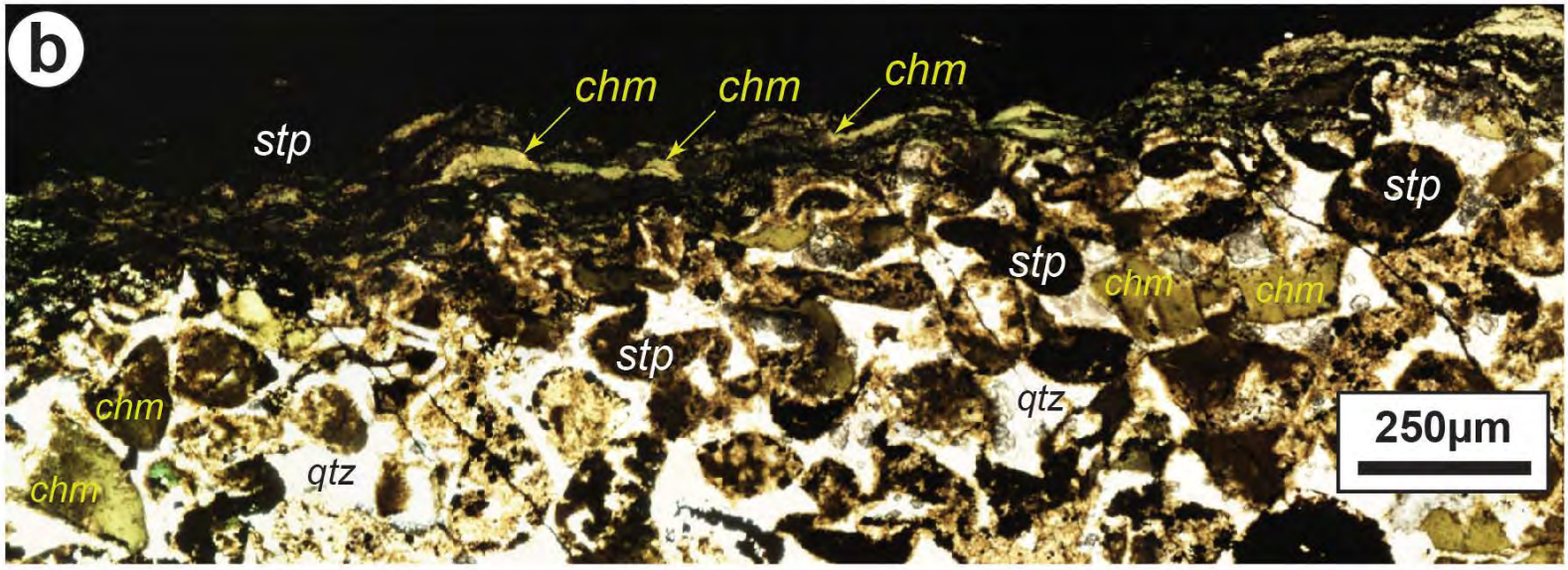
b
chm
chm
chm
stp
stp
stp
chm
chm
stp
qtz
chm
chm
qtz
250µm
banded
Si-cemented

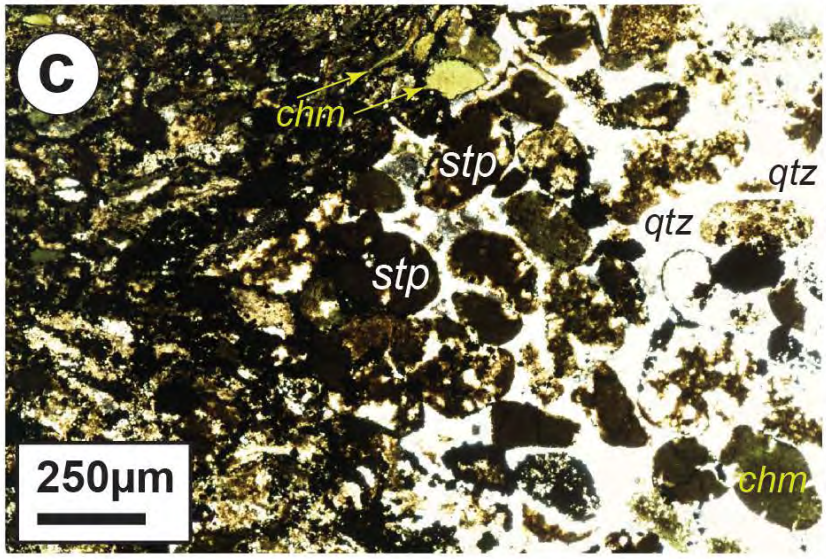
c
chm
stp
qtz
qtz
stp
250µm
chm

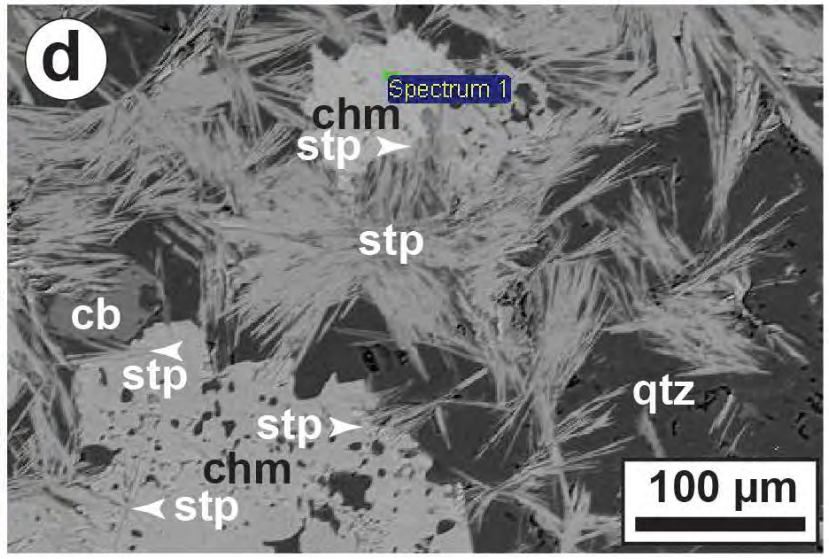
d
Spectrum 1
chm
stp
stp
cb
stp
qtz
stp
chm
stp
100 µm

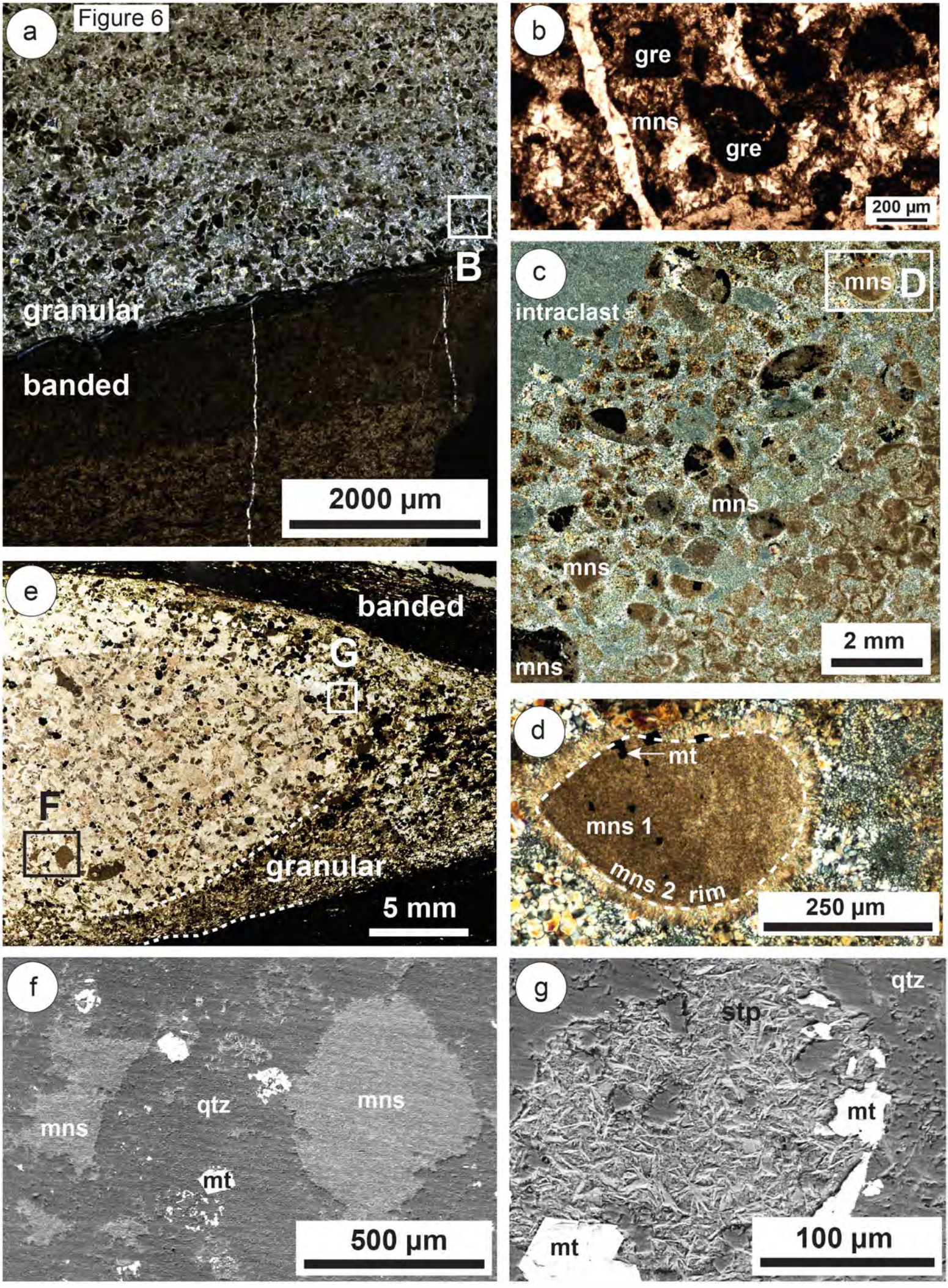
a
Figure 6
B
granular
banded
2000 µm
b
gre
mns
gre
200 µm
c
intraclast
mns D
mns
mns
mns
2 mm
d
mt
mns 1
mns 2 rim
250 µm
e
banded
G
F
granular
5 mm
f
mns
qtz
mns
mt
500 µm
g
qtz
stp
mt
mt
100 µm

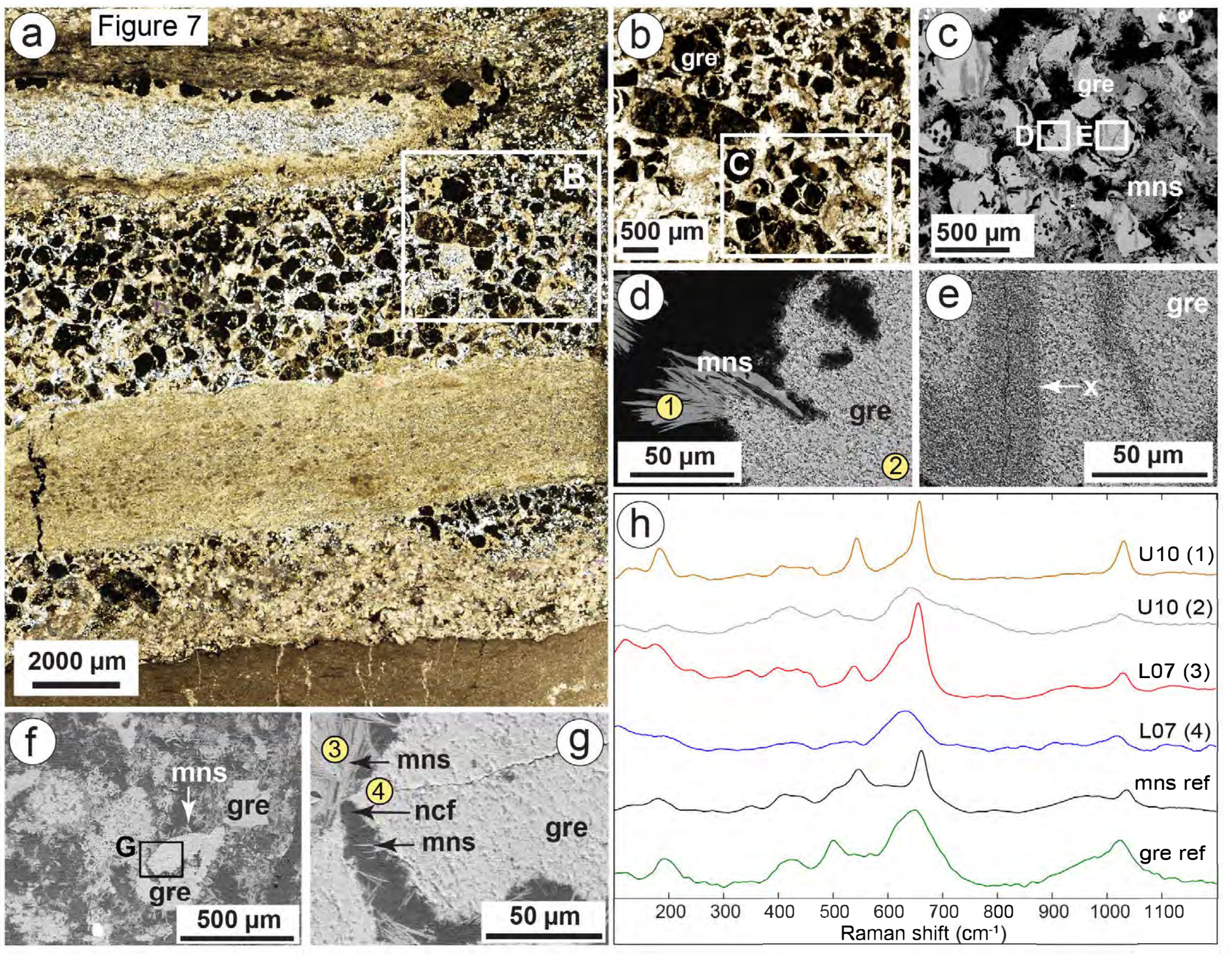
a
Figure 7
B
2000 µm
b
gre
C
500 µm
c
gre
D
E
mns
500 µm
d
mns
1
gre
50 µm
2
e
gre
x
50 µm
h
U10 (1)
U10 (2)
L07 (3)
L07 (4)
mns ref
gre ref
200 300 400 500 600 700 800 900 1000 1100
Raman shift (cm-1)
f
mns
gre
G
gre
500 µm
g
3
mns
4
ncf
mns
gre
50 µm

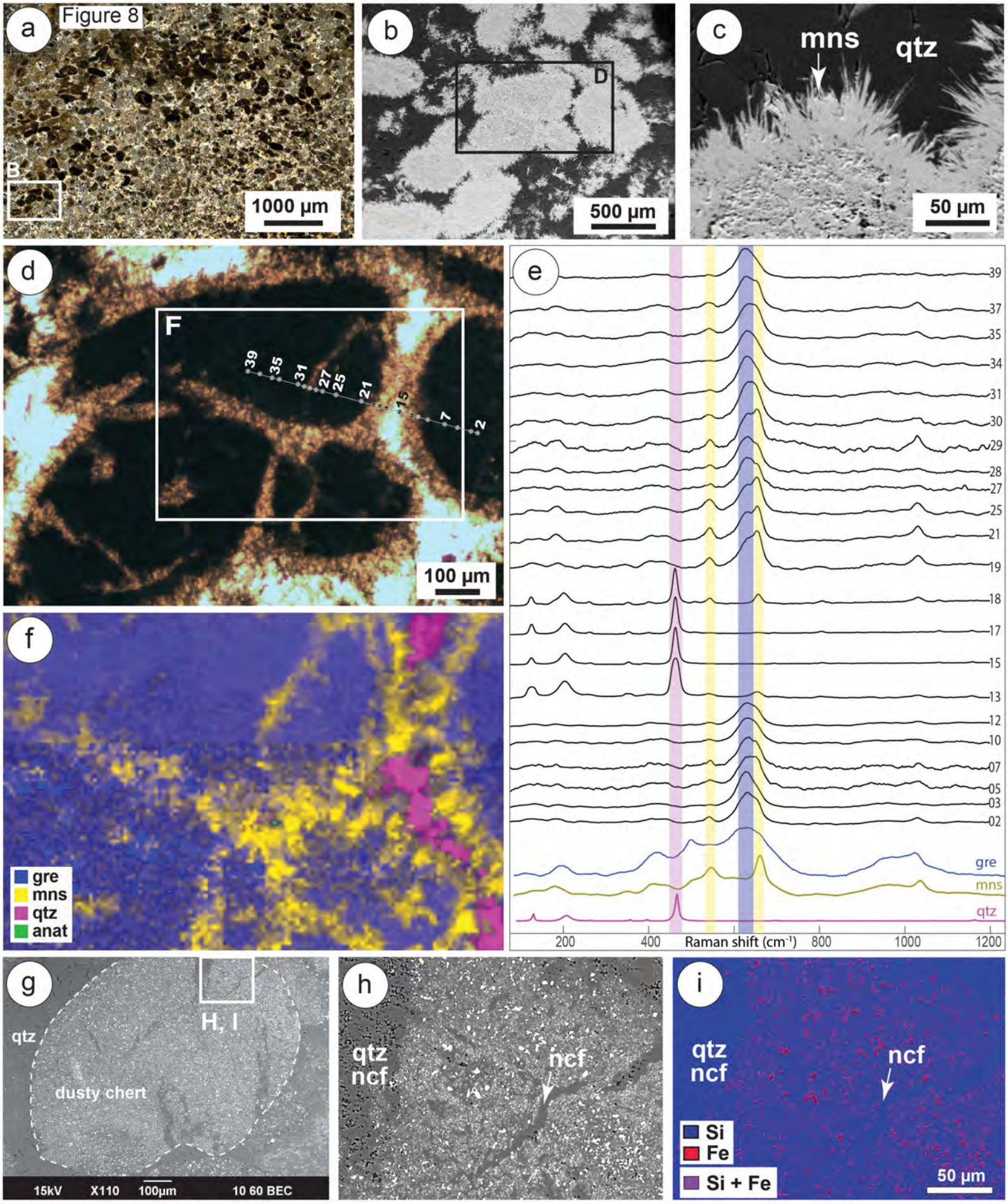
a
Figure 8
B
1000 µm
b
D
500 µm
c
mns
qtz
50 µm
d
F
39
35
31
27
25
21
15
7
2
100 µm
e
39
37
35
34
31
30
29
28
27
25
21
19
18
17
15
13
12
10
07
05
03
02
gre
mns
qtz
200
400
Raman shift (cm-1)
800
1000
1200
f
gre
mns
qtz
anat
g
H, I
qtz
dusty chert
15kV X110 100µm 10 60 BEC
h
qtz
ncf
ncf
i
qtz
ncf
ncf
Si
Fe
Si + Fe
50 µm

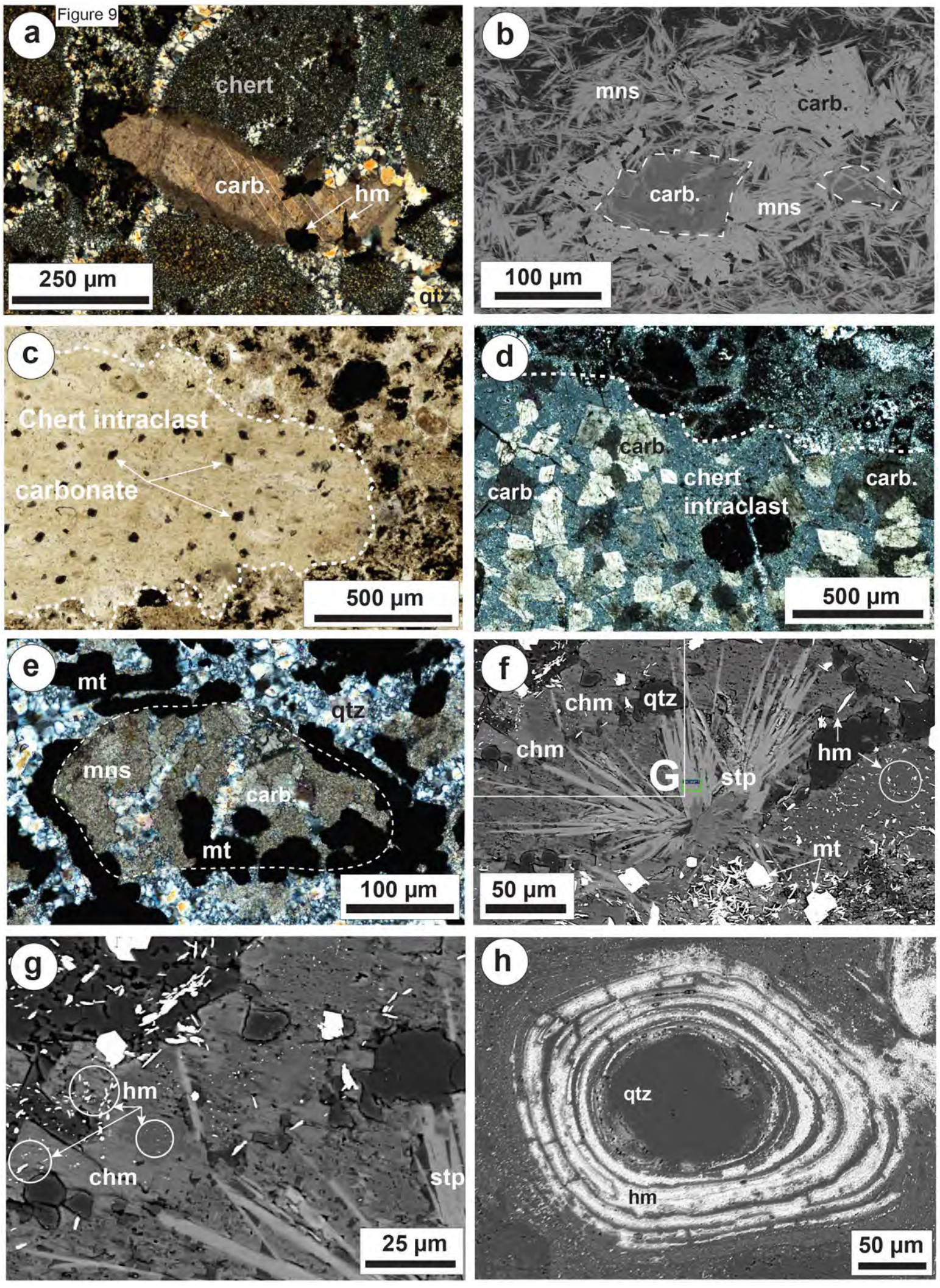
Figure 9
a
chert
carb.
hm
250 µm
qtz
b
mns
carb.
carb.
mns
100 µm
c
Chert intraclast
carbonate
500 µm
d
carb
carb
chert
intraclast
carb.
500 µm
e
mt
qtz
mns
carb.
mt
100 µm
f
chm
qtz
chm
G
stp
hm
mt
50 µm
g
hm
chm
stp
25 µm
h
qtz
hm
50 µm

Figure 10

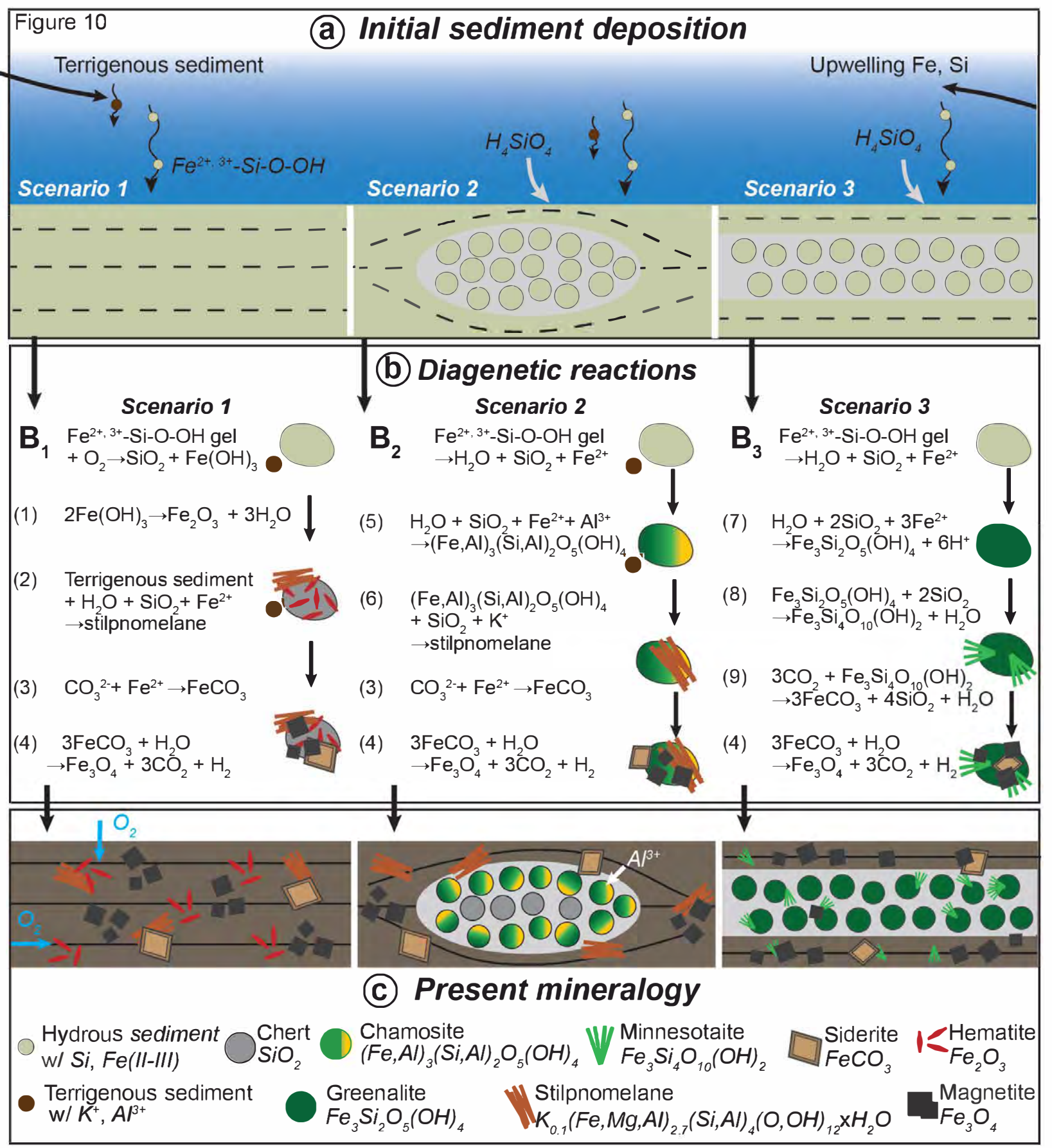
a Initial sediment deposition
Terrigenous sediment
Upwelling Fe, Si
$Fe^{2+, 3+}$-Si-O-OH
H_4SiO_4
H_4SiO_4
Scenario 1
Scenario 2
Scenario 3
b Diagenetic reactions
Scenario 1
Scenario 2
Scenario 3
B1 $Fe^{2+, 3+}$-Si-O-OH gel + $O_2 \rightarrow SiO_2 + Fe(OH)_3$
(1) $2Fe(OH)_3 \rightarrow Fe_2O_3 + 3H_2O$
(2) Terrigenous sediment + $H_2O + SiO_2 + Fe^{2+}$ →stilpnomelane
(3) $CO_3^{2-} + Fe^{2+} \rightarrow FeCO_3$
(4) $3FeCO_3 + H_2O \rightarrow Fe_3O_4 + 3CO_2 + H_2$
B2 $Fe^{2+, 3+}$-Si-O-OH gel $\rightarrow H_2O + SiO_2 + Fe^{2+}$
(5) $H_2O + SiO_2 + Fe^{2+} + Al^{3+} \rightarrow (Fe,Al)_3(Si,Al)_2O_5(OH)_4$
(6) $(Fe,Al)_3(Si,Al)_2O_5(OH)_4 + SiO_2 + K^+$ →stilpnomelane
(3) $CO_3^{2-} + Fe^{2+} \rightarrow FeCO_3$
(4) $3FeCO_3 + H_2O \rightarrow Fe_3O_4 + 3CO_2 + H_2$
B3 $Fe^{2+, 3+}$-Si-O-OH gel $\rightarrow H_2O + SiO_2 + Fe^{2+}$
(7) $H_2O + 2SiO_2 + 3Fe^{2+} \rightarrow Fe_3Si_2O_5(OH)_4 + 6H^+$
(8) $Fe_3Si_2O_5(OH)_4 + 2SiO_2 \rightarrow Fe_3Si_4O_{10}(OH)_2 + H_2O$
(9) $3CO_2 + Fe_3Si_4O_{10}(OH)_2 \rightarrow 3FeCO_3 + 4SiO_2 + H_2O$
(4) $3FeCO_3 + H_2O \rightarrow Fe_3O_4 + 3CO_2 + H_2$
O_2
O_2
Al^{3+}
c Present mineralogy
Hydrous sediment w/ Si, Fe(II-III)
Chert SiO_2
Chamosite $(Fe,Al)_3(Si,Al)_2O_5(OH)_4$
Minnesotaite $Fe_3Si_4O_{10}(OH)_2$
Siderite $FeCO_3$
Hematite Fe_2O_3
Terrigenous sediment w/ K^+, Al^{3+}
Greenalite $Fe_3Si_2O_5(OH)_4$
Stilpnomelane $K_{0.1}(Fe,Mg,Al)_{2.7}(Si,Al)_4(O,OH)_{12}xH_2O$
Magnetite Fe_3O_4